Monthly Notices of the ROYAL ASTRONOMICAL SOCIETY

MNRAS **523,** 2083–2110 (2023)
Advance Access publication 2023 May 22

https://doi.org/10.1093/mnras/stad1532

Star cluster formation from turbulent clumps – III. Across the mass spectrum

Juan P. Farias [1,2]★ and Jonathan C. Tan[1,3]

[1]*Department of Space, Earth & Environment, Chalmers University of Technology, SE-41293 Gothenburg, Sweden*
[2]*Department of Astronomy, University of Texas at Austin, Austin, TX 78712, USA*
[3]*Department of Astronomy, University of Virginia, Charlottesville, VA 22904, USA*

Accepted 2023 May 12. Received 2023 April 12; in original form 2023 January 23

ABSTRACT

We study the formation and early evolution of star clusters that have a wide range of masses and background cloud mass surface densities, $\Sigma_{\rm cloud}$, which help set the initial sizes, densities, and velocity dispersions of the natal gas clumps. Initial clump masses of 300, 3000, and 30 000 $M_\odot$ are considered, from which star clusters are born with an assumed 50 per cent overall star formation efficiency and with 50 per cent primordial binarity. This formation is gradual, i.e. with a range of star formation efficiencies per free-fall time from 1 to 100 per cent, so that the formation time can range from 0.7 Myr for low-mass, high-$\Sigma_{\rm cloud}$ clumps to $\sim$30 Myr for high-mass, low-$\Sigma_{\rm cloud}$ clumps. Within this framework of the turbulent clump model, for a given $\Sigma_{\rm cloud}$, clumps of higher mass are of lower initial volume density, but their dynamical evolution leads to higher bound fractions and causes them to form much higher density cluster cores and maintain these densities for longer periods. This results in systematic differences in the evolution of binary properties, degrees of mass segregation, and rates of creation of dynamically ejected runaways. We discuss the implications of these results for observed star clusters and stellar populations.

Key words: methods: numerical – galaxies: star clusters: general – stars: kinematics and dynamics – stars: formation.

1 INTRODUCTION

Most stars appear to form in clusters (or at least initially clustered associations) inside molecular clouds (e.g. Gutermuth et al. 2009). A wide range of scales is involved, including the broad distribution of cluster masses that make up the initial cluster mass function (ICMF). For masses $\gtrsim$100 $M_\odot$ and up to at least $\sim10^5$ $M_\odot$, the ICMF appears to follow a power law of the form $dN/d\log M \propto M^{-1}$ (e.g. Lada & Lada 2003; Dowell, Buckalew & Tan 2008), so that there is an equal mass contributed by clusters in each decade of the mass spectrum. Thus considering a broad range of cluster masses is needed when understanding the origin of galactic stellar populations.

Star cluster formation itself is a very complex process that involves the interplay of many physical processes, including fragmentation of self-gravitating, turbulent, magnetized molecular clouds, protostellar outflow feedback from accreting stars (e.g. Nakamura & Li 2007; Cunningham et al. 2011; Hansen et al. 2012; Federrath et al. 2014; Nakamura & Li 2014; Geen et al. 2015), other feedback processes from already formed, especially massive, stars (e.g. Peters et al. 2010, 2011; Rogers & Pittard 2013; Dale, Ercolano & Bonnell 2015), and dynamical evolution of the stellar population, including dynamical ejection of runaway stars (e.g. Banerjee, Kroupa & Oh 2012; Oh & Kroupa 2016; Gavagnin et al. 2017). All these processes have their own spatial regimes and time-scales over which they are important.

It is not currently possible to include all the above processes in a unified simulation to model star cluster formation. Our approach, developed in a series of papers of which this is the third, explores star cluster formation within the paradigm of the turbulent core/clump model (McKee & Tan 2003) with approximate implementation of the birth of stars via their gradual introduction into simulations that follow the N-body dynamical evolution of the system. The overall goal is to explore how the stellar population, including realistic binary properties, is processed dynamically during the formation phase of a star cluster, and how this processing may be affected by model parameters. There are two basic parameters describing the initial star-forming clumps: the clump mass, $M_{\rm cl}$, and the mass surface density of the surrounding 'cloud' environment, $\Sigma_{\rm cloud}$, which sets the bounding pressure of the clumps and thus their radii, $R_{\rm cl}$. High-$\Sigma_{\rm cloud}$ environments have high pressures, i.e. due to the self-gravity of the cloud, which means that clumps of a given mass are denser in such environments. The formation phase of the cluster also involves two main parameters: the star formation efficiency per free-fall time, $\epsilon_{\rm ff}$, and the overall star formation efficiency of the clump, ϵ.

In Farias, Tan & Chatterjee (2017, hereafter Paper I), we first explored an extreme version of this scenario in which the star clusters are formed instantaneously from their parent clumps. While instantaneous formation appears to be an unrealistic case, we note that this has been the standard practice in almost all such similar studies so far (with the notable exception of Proszkow & Adams 2009). In our second work of this series, Farias, Tan & Chatterjee (2019, hereafter Paper II), we implemented gradual formation of stars, which enabled us to explore a wide range of formation time-scales (achieved via a range of values of $\epsilon_{\rm ff}$ and a fixed, fiducial value of $\epsilon = 0.5$). We showed that such time-scales strongly influence the dynamical evolution of the clusters in both the embedded phase (i.e.

★ E-mail: juan.farias@austin.utexas.edu

when gas is still present) and during the subsequent gas-free phase, including the rate and amount of expansion, the fraction of stars that remain bound, the frequency of ejection events, the establishment of age-radius gradients and the degree of processing of binaries.

However, in these previous papers we limited the studies to a fixed parent clump mass of 3000 $M_\odot$. It is not immediately obvious how our results would scale with mass (at a fixed $\Sigma_{\rm cloud}$), since there are several coupled processes at play with various different time-scales and dependencies. Thus, our goal in this paper is to present a series of *N*-body simulations that explore different clump masses using the same framework as in Paper II. These simulations will help us to elucidate how the various dynamical processes, described above, combine to control the dynamical evolution of clusters across the mass spectrum.

2 THEORETICAL BACKGROUND

2.1 Background gas model

We perform star cluster formation simulations following the methods presented in Paper I and Paper II. In these models, star clusters are assumed to be forming from gravitationally bound, initially starless gas clumps within giant molecular clouds (GMCs), partially supported by magnetic fields and turbulence. The structure of the parent clumps is described following the turbulent core/clump model of McKee & Tan (2003), i.e. they are polytropic spheres in virial and pressure equilibrium with their surroundings. The density profile of such clumps is modelled as

$$\rho_{\rm cl}(r) = \rho_{\rm s,cl}\left(\frac{r}{R_{\rm cl}}\right)^{-k_\rho}, \tag{1}$$

and the velocity dispersion profile as

$$\sigma_{\rm cl}(r) = \sigma_{\rm s}\left(\frac{r}{R_{\rm cl}}\right)^{(2-k_\rho)/2}, \tag{2}$$

where $\rho_{\rm s,cl}$ and $\sigma_{\rm s}$ are the density and velocity dispersion at the surface of the clump, respectively, $R_{\rm cl}$ is the clump radius, i.e. where its boundary is located, and we adopt $k_\rho = 1.5$ as the fiducial power law of the density distribution (e.g. Butler & Tan 2012). One important feature to note is that the velocity dispersion increases with radius (see McKee & Tan 2003), which is a general feature of interstellar turbulence. We refer the reader to Paper I and Paper II, where we discuss the dynamical implications of such a characteristic for the formation and evolution of our model star clusters.

Using our fiducial parameters for the structure of the parent clump, the characteristic radius and velocity dispersion at the clump surface are controlled by the surrounding cloud's mass surface density, $\Sigma_{\rm cloud}$, and are given by

$$R_{\rm cl} = 0.365\left(\frac{M_{\rm cl}}{3000\,{\rm M}_\odot}\right)^{1/2}\left(\frac{\Sigma_{\rm cloud}}{1\,{\rm g\,cm^{-2}}}\right)^{-1/2}{\rm pc}, \tag{3}$$

and

$$\sigma_{\rm s} = 3.04\left(\frac{M_{\rm cl}}{3000\,{\rm M}_\odot}\right)^{1/4}\left(\frac{\Sigma_{\rm cloud}}{1\,{\rm g\,cm^{-2}}}\right)^{1/4}{\rm km\,s^{-1}}. \tag{4}$$

Following our previous works, we model clumps in two different cloud environments: the high-Σ case with $\Sigma_{\rm cloud} = 1.0\,{\rm g\,cm^{-2}}$ and the low-Σ case with $\Sigma_{\rm cloud} = 0.1\,{\rm g\,cm^{-2}}$. Such a range is likely to be relevant for a large fraction of the star-forming systems of our Galaxy (Tan et al. 2014): for example, large portions of the samples of the infrared dark cloud clumps of Butler & Tan (2012), of the high-mass star-forming clumps of Mueller et al. (2002), and the massive clumps of Ginsburg et al. (2012) are in or near this region of parameter space. Then, given $R_{\rm cl}$, defined by $M_{\rm cl}$ and $\Sigma_{\rm cloud}$, the density at the surface of the clump is

$$\rho_{\rm s,cl} = \frac{(3-k_\rho)M_{\rm cl}}{4\pi R_{\rm cl}^3}. \tag{5}$$

In Paper II, we introduced models of gradual formation of star clusters, i.e. in which natal gas is still present while stars are being formed. The influence of the natal gas in the evolution of the forming star cluster is modelled as a time-dependent background potential derived from equation (1), i.e.

$$\Phi_{\rm gas}(r,t) = \begin{cases} \dfrac{GM_{\rm cl}(t)}{(2-k_\rho)R_{\rm cl}}\left[\left(\dfrac{r}{R_{\rm cl}}\right)^{2-k_\rho} - 3 + k_\rho\right] & (r \le R_{\rm cl}) \\ -\dfrac{GM_{\rm cl}(t)}{r} & (r > R_{\rm cl}) \end{cases}, \tag{6}$$

where G is the gravitational constant and $M_{\rm cl}(t)$ the time-dependent clump gas mass. Note the radius of the clump is truncated at $R_{\rm cl}$ and no additional gas mass is modelled beyond this radius, i.e. no further contributions to the potential are made from the surrounding cloud.

We keep our previous assumption of a constant star formation rate (SFR) defined using the *initial* parameters of the clump, i.e.

$$\dot{M}_* = \frac{\epsilon_{\rm ff} M_{\rm cl,0}}{t_{\rm ff,0}}, \tag{7}$$

where the initial free-fall time of the clump, $t_{\rm ff,0}$, is also defined by $\Sigma_{\rm cloud}$ and $M_{\rm cl,0}$. Using the fiducial clump parameters, it is given by

$$t_{\rm ff,0} = 0.069\left(\frac{M_{\rm cl,0}}{3000\,{\rm M}_\odot}\right)^{1/4}\left(\frac{\Sigma_{\rm cloud}}{1\,{\rm g\,cm^{-2}}}\right)^{-3/4}{\rm Myr}. \tag{8}$$

We assume that there is a local star formation efficiency, ϵ, i.e. defined as the ratio between the stellar mass formed and the total mass required to form such a stellar mass. The fiducial value of $\epsilon = 0.5$ with such a value being typical of expectations of local star formation efficiency from individual pre-stellar cores due to protostellar outflow feedback (e.g. Matzner & McKee 2000; Tanaka, Tan & Zhang 2017). For simplicity, the gas that does not make it into a star is assumed to be instantaneously lost from the clump. We assume star formation proceeds in this way until all the gas from the clump is exhausted. Therefore, the time evolution of the global gaseous mass of the clump is given by

$$M_{\rm cl}(t) = \begin{cases} M_{\rm cl,0} - \dfrac{\dot{M}_*}{\epsilon}t & (t \le t_*) \\ 0 & (t > t_*), \end{cases} \tag{9}$$

where t_* is the time at which gas is exhausted. Since we assume a constant SFR, the formation time is given by

$$t_* = \frac{\epsilon}{\epsilon_{\rm ff}}t_{\rm ff,0} \propto \frac{\epsilon}{\epsilon_{\rm ff}}\left(\frac{M_{\rm cl}}{\Sigma_{\rm cloud}^3}\right)^{1/4}. \tag{10}$$

2.2 Scaling of clump properties with mass

In this work, we explore how the formation and early evolution of star clusters depends on the initial mass of the clump, $M_{\rm cl}$. Within the context of the turbulent clump model, several important parameters and features of the clumps and clusters vary with clump mass, which we overview in Fig. 1. In particular, this figure shows how several clump properties vary with $M_{\rm cl}$, while keeping the bounding cloud mass surface density, $\Sigma_{\rm cloud}$, constant. Values are normalized relative to the $M_{\rm cl} = 3000\,{\rm M}_\odot$ case (and numerical values shown in the

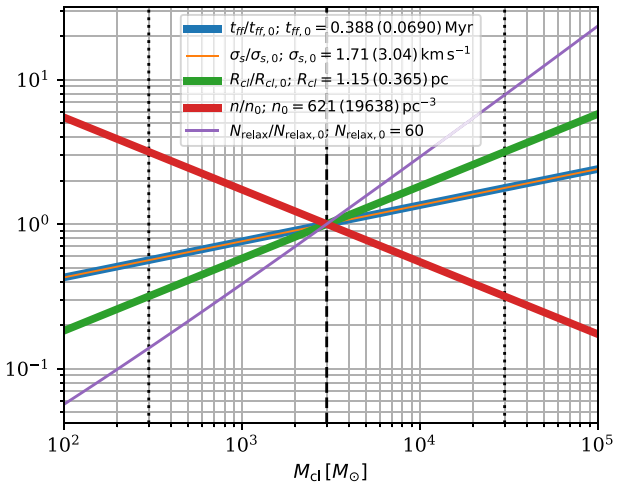

Figure 1. Variation of global clump parameters with mass, normalized with respect to clumps with $M_{cl} = 3000\,M_\odot$. Legend shows fiducial values for this case with $\Sigma_{cloud} = 0.1\,g\,cm^{-2}$ and $\Sigma_{cloud} = 1\,g\,cm^{-2}$ in parenthesis. Dotted vertical lines show the masses of the new models introduced in this paper with 300 and 30 000 $M_\odot$.

legend of the figure apply for the model with $\Sigma_{cloud} = 0.1\,g\,cm^{-2}$). Naturally, increasing the mass of the clump requires a larger clump radius to keep mass surface density constant (there is a one-to-one relation of clump mass surface density and surrounding cloud mass surface density; McKee & Tan 2003), with $R_{cl} \propto M_{cl}^{1/2}$ (thick green line). From equation (3), we see that the one-dimensional velocity dispersion at the surface of the clump, σ_s, scales with mass as $\sigma_s \propto M_{cl}^{1/4}$. Thus, the crossing time varies as $t_{cr} \propto R_{cl}/\sigma_s \propto M_{cl}^{1/4}$. The same scaling applies to the free-fall time $t_{ff} \propto M_{cl}^{1/4}$ (see equation 8).

For fixed star formation efficiency, the number density of stars that would be initially contained in the volume of the clump scales as $n_* \propto M_{cl}/R_{cl}^3 \propto M_{cl}^{-1/2}$. Defining N_{relax} as the relaxation time, t_{relax}, divided by the crossing time, it is known that $N_{relax} \propto M_{cl}/\ln M_{cl}$ (see Binney & Tremaine 2008). A star cluster needs to evolve for about N_{relax} crossing times for the individual stars to lose information of their initial orbits and reach a near dynamical equilibrium state. Thus, a more massive cluster takes longer (both in terms of number of crossing times and in terms of absolute time) to reach an equilibrium configuration. This is relevant since the initial state of the stars that are formed from the turbulent clump model are not in the equilibrium configuration of a gas-free stellar cluster. Finally, for fixed values of ϵ and ϵ_{ff}, the formation time-scales as $t_* \propto t_{ff} \propto M_{cl}^{1/4}$.

3 METHODS

3.1 Gradual formation of stars

In this paper, matching the examples of Paper II, we will follow the formation and early evolution of star clusters for up to about 20 Myr. This involves a formation phase, i.e. when gas is still present, and then a post-formation, gas-free phase. During the formation phase, as the background gas model evolves, stars are gradually introduced in the simulations according to the previously calculated constant SFR following the same phase-space distribution of the gas. As introduced in Paper II, we include this prescription in a modified version of the direct N-body code NBODY6++ (Aarseth 2003; Wang et al. 2015), where we are able to introduce stars, including primordial binaries, at arbitrary times during runtime. The minimum number of stars we can model with this code is of the order of 150, which is the initial number of stars all models start with. The primordial binary fraction in a given simulation is held constant in time, so that if no binaries are disrupted, then the total binary fraction would, on average, remain constant during star formation.

As in Paper I and Paper II, stellar mass-loss from stellar evolution was included in the simulations using the analytical models developed by Hurley, Pols & Tout (2000); Hurley, Tout & Pols (2002) implemented in NBODY6++, including mass transfer between binaries and close interacting stars, so that the full stellar evolutionary path is not simply defined by the initial mass and metallicity, but can change with the dynamical history of the stars. We note that these stellar evolutionary models do not include the pre-main-sequence phase, when stars are generally larger than their main-sequence sizes, so that such interactions will tend to be underestimated somewhat. However, in general, close interactions between stars occur only very rarely in our simulations and this limitation is not expected to influence the overall results significantly. The models also include velocity kicks for neutron stars (but not black holes) that are formed from asymmetrical supernovae ejections. The magnitude of the kicks follows a Maxwellian velocity distribution with $\sigma = 265\,km\,s^{-1}$, based on proper motion observations of runaway pulsars (Hobbs et al. 2005).

3.2 Primordial stellar population

In this work, we aim to isolate the effects of the different parent clump masses and so we use a stellar population that is identical to the fiducial set of simulations in our previous works. This uses a canonical initial mass function (IMF; Kroupa 2001) with 50 per cent binaries in circular orbits. We construct the binary population from a lognormal period distribution with a mean of $P = 293$ yr and standard deviation of $\sigma_{\log P} = 2.28$ according to observations of Raghavan et al. (2010). The mass ratio distribution follows the form $dN/dq \propto q^{0.7}$ as observed in young star clusters (Reggiani & Meyer 2011). The binary population is constructed from the full set of individual stars (binary members and singles) that follows the adopted IMF. We note that this construction implies that in general low-mass stars end up with slightly higher binary fractions than more massive stars. This is because once a primary star is selected, the companion, which has a lower mass by construction, is selected according to the mass ratio distribution. Therefore, low-mass stars have higher chances of being selected to be part of a binary system. In our scheme, brown dwarfs then have primordial binary fractions of 60 per cent, while stars above 0.4 $M_\odot$ have 40 per cent primordial binary fractions resulting in an average of 50 per cent. We note that this disagrees with observations where most massive stars tend to have higher multiplicity fractions (Offner et al. 2022). However, it is possible that such a trend develops dynamically after the formation phase, which we will assess in a future work in this series.

3.3 Different mass models

We perform two sets of simulations, i.e. with clump masses 10 times greater and 10 times smaller than the clumps of Paper II which had $M_{cl} = 3000\,M_\odot$. To make the sets statistically comparable, we carry out 200 simulations with $M_{cl} = 300\,M_\odot$ and 2 simulations with $M_{cl} = 30\,000\,M_{cl}$ for each value of $\Sigma_{cloud} = 0.1$ and $1\,g\,cm^{-2}$ (hereafter low- and high-Σ_{cloud} cases, respectively). We compare these to 20 simulations of Paper II for each Σ_{cloud} case. All the simulations used for this comparison have a global star formation efficiency, $\epsilon =$ 50 per cent. We also explore a range star formation efficiency per

Table 1. Simulations parameters.

Set name	$\epsilon_{\rm ff}$	$\Sigma_{\rm cloud}$ ($\rm g\,cm^{-2}$)	$M_{\rm cl}$ ($\rm M_\odot$)	$\langle N_* \rangle$	t_* (Myr)	$t_{\rm ff}$ (Myr)	$R_{\rm cl}$ (pc)	$\sigma_{\rm s}$ ($\rm km\,s^{-1}$)
m300L	0.01	0.1	300	400	10.91	0.22	0.36	0.96
	0.03	0.1	300	400	3.64	0.22	0.36	0.96
	0.1	0.1	300	400	1.09	0.22	0.36	0.96
	0.3	0.1	300	400	0.36	0.22	0.36	0.96
	1.0	0.1	300	400	0.11	0.22	0.36	0.96
m3000L	0.01	0.1	3000	4000	19.40	0.39	1.15	1.71
	0.03	0.1	3000	4000	6.47	0.39	1.15	1.71
	0.1	0.1	3000	4000	1.94	0.39	1.15	1.71
	0.3	0.1	3000	4000	0.65	0.39	1.15	1.71
	1.0	0.1	3000	4000	0.19	0.39	1.15	1.71
m30000L	0.01	0.1	30 000	40 000	34.50	0.69	3.65	3.04
	0.03	0.1	30 000	40 000	11.50	0.69	3.65	3.04
	0.1	0.1	30 000	40 000	3.45	0.69	3.65	3.04
	0.3	0.1	30 000	40 000	1.15	0.69	3.65	3.04
	1.0	0.1	30 000	40 000	0.34	0.69	3.65	3.04
m300H	0.01	1.0	300	400	1.94	0.039	0.115	1.71
	0.03	1.0	300	400	0.65	0.039	0.115	1.71
	0.1	1.0	300	400	0.19	0.039	0.115	1.71
	0.3	1.0	300	400	0.06	0.039	0.115	1.71
	1.0	1.0	300	400	0.02	0.039	0.115	1.71
m3000H	0.01	1.0	3000	4000	3.45	0.069	0.365	3.04
	0.03	1.0	3000	4000	1.15	0.069	0.365	3.04
	0.1	1.0	3000	4000	0.35	0.069	0.365	3.04
	0.3	1.0	3000	4000	0.12	0.069	0.365	3.04
	1.0	1.0	3000	4000	0.03	0.069	0.365	3.04
m30000L	0.01	1.0	30 000	40 000	6.14	0.123	1.154	5.41
	0.03	1.0	30 000	40 000	2.05	0.123	1.154	5.41
	0.1	1.0	30 000	40 000	0.61	0.123	1.154	5.41
	0.3	1.0	30 000	40 000	0.20	0.123	1.154	5.41
	1.0	1.0	30 000	40 000	0.06	0.123	1.154	5.41

free-fall time with the same values as in Paper II, i.e. $\epsilon_{\rm ff} = 0.01$, 0.03, 0.1, 0.3, and 1. Table 1 shows the simulation parameters for the different simulations performed. For the most massive clusters, we have utilized GPUs to run the simulations to be able to access greater computational resources and run the calculations more efficiently. This large set of simulations was scheduled using the automated Simulation Monitor for Computational Astrophysics, SiMon (Qian et al. 2017).

4 RESULTS

4.1 Evolution of global structure and kinematics

Fig. 2 shows the evolution of the Lagrangian radii of the star clusters with reference to all the stars in the system (solid lines), along with the bound stellar component (shaded regions), for our fiducial choice of $\epsilon_{\rm ff} = 0.03$. We see that during the formation stage, when the gas is still present, the clusters tend to be confined by its gravitational potential. This behaviour was already noted for the $M_{\rm cl} = 3000\,\rm M_\odot$ case in Paper II. After star formation is completed, then the clusters expand more quickly. This phase begins earlier for lower mass and higher density clusters (see Table 1). Fig. 2 also shows the evolution of the cluster core radii, discussed in more detail below.

We next consider the effect of varying $\epsilon_{\rm ff}$ on the evolution of the clusters. Figs 3 and 4 show the evolution of the different parameters for the low- and high-$\Sigma_{\rm cloud}$ cases, respectively. In each figure, the first, second, and third columns show results for star clusters forming from clumps with $M_{\rm cl} = 300$, 3000, and $30\,000\,\rm M_\odot$, respectively, while the fourth column shows the three cases together for the fiducial value of $\epsilon_{\rm ff} = 0.03$.

The top rows of Figs 3 and 4 show the evolution of the bound mass fraction, $f_{\rm bound}$. The values of $f_{\rm bound}$ of the various models are quite similar at the end of the formation time, which is determined mainly by $\Sigma_{\rm cloud}$ and $\epsilon_{\rm ff}$, but also by $M_{\rm cl}$ to a lesser degree (see equation 10).

In the post-formation phase, cluster dissolution and evaporation effects then occur. The rates of these processes are mostly driven by the rate of cluster relaxation, with lower mass clusters evolving more quickly to smaller bound fractions. For example, by 20 Myr in the high-$\Sigma_{\rm cloud}$ case, the clusters formed from $M_{\rm cl} = 300\,\rm M_\odot$ clumps have bound fractions of only about 0.3, i.e. these are very low mass clusters with bound stellar masses of only $\sim$50 $\rm M_\odot$. In the low-$\Sigma_{\rm cloud}$ case, these low-mass clusters have higher bound fractions at 20 Myr, with values of $\sim$0.5, mostly because their formation took longer and the post-formation phase is a smaller fraction of the 20 Myr evolution. Considering the $M_{\rm cl} = 3000\,\rm M_\odot$ cases, the bound fractions at 20 Myr are higher, i.e. $\sim$0.6 in the low-density models and $\sim$0.7 in the high-density models, but with some dispersion caused by $\epsilon_{\rm ff}$. These higher bound fractions are caused, at least in part, by the cluster relaxation times being significantly longer. These general trends continue up to the $M_{\rm cl} = 30\,000\,\rm M_\odot$ cases, which retain the highest bound fractions at 20 Myr of $\sim$0.8 for the fiducial $\epsilon_{\rm ff} = 0.03$ case. This corresponds to a star cluster of mass $\sim$12 000 $\rm M_\odot$.

The second rows of Figs 3 and 4 show the evolution of bound cluster half-mass radii, $r_{\rm h,b}$, while the third rows show the evolution of the average number density of stars, evaluated inside these radii. We see that $r_{\rm h,b}$ remains quite constant during the formation phase,

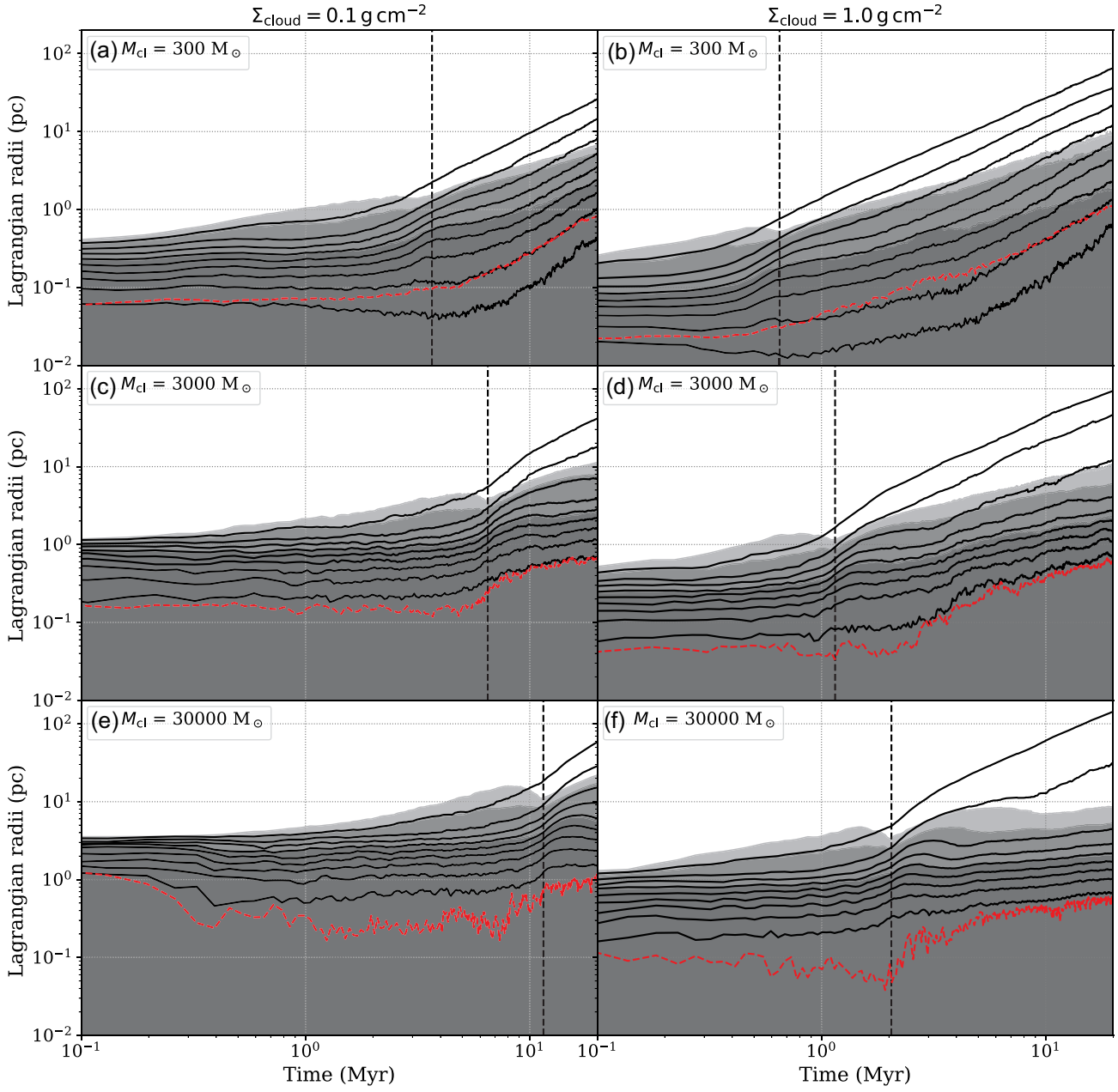

Figure 2. Time evolution of Lagrangian radii enclosing 10, 20, 30, 40, 50, 60, 70, 80, and 90 per cent of the stellar mass for star clusters with different $M_{\rm cl}$ (top, middle, and bottom rows, as labelled), formed with $\epsilon = 0.5$ and $\epsilon_{\rm ff} = 0.03$. Left-hand panels shows the low-$\Sigma_{\rm cloud}$ case and right-hand panels the respective simulations for the high-$\Sigma_{\rm cloud}$ case. The lines show the averages over all the simulations performed in each set. Background shaded areas show the average Lagrangian radii for the 50, 80, and 90 per cent bound stellar masses. Dashed red lines show the average core radii. Vertical dashed lines show the respective gas exhaustion time t_*.

and then undergoes expansion once the gas has been exhausted. The low-mass clusters end their formation with radii of $r_{\rm h,b} \sim 0.1$–0.3 pc. The clusters forming relatively quickly, i.e. with $\epsilon_{\rm ff} \gtrsim 0.1$, have a chance to enter a 'post-formation stabilization' (PFS) phase, when $r_{\rm h,b}$ stays at a nearly constant level, i.e. $r_{\rm h,b,\,PFS}$, that is about a factor of 2 to 3 greater than during formation. After this the clusters undergo very dramatic expansion, driven by dynamical relaxation. Note that the slow-forming models do not have a chance to enter the PFS phase, since they are still forming when dynamical relaxation starts to drive their expansion. The low-mass clusters reach sizes of about 2 pc in the low-density case and about 5 pc in the high-density case, which thus, in fact, achieve the lowest number density of stars of any of our models, i.e. only $\sim$10 pc^{-3}, after a decline of about a factor of 10^4. The effects of $\epsilon_{\rm ff}$ are relatively modest on the values of $r_{\rm h,b}$ reached by 20 Myr, with the main differences occurring at earlier times around $\sim$ 1 Myr due to the different durations of the formation phases and whether or not they have a chance to enter the PFS phase.

These general trends continue for the $M_{\rm cl} = 3000\,{\rm M}_\odot$ cases, though with the variation in sizes due to different onsets of the PFS phases shifted to somewhat later times, ranging from about 0.5 to 2 Myr with $r_{\rm h,b,PFS} \simeq 0.7$ pc in the high-density environments and about 2 to 5 Myr with $r_{\rm h,b,PFS} \simeq 2$ pc in the low-density

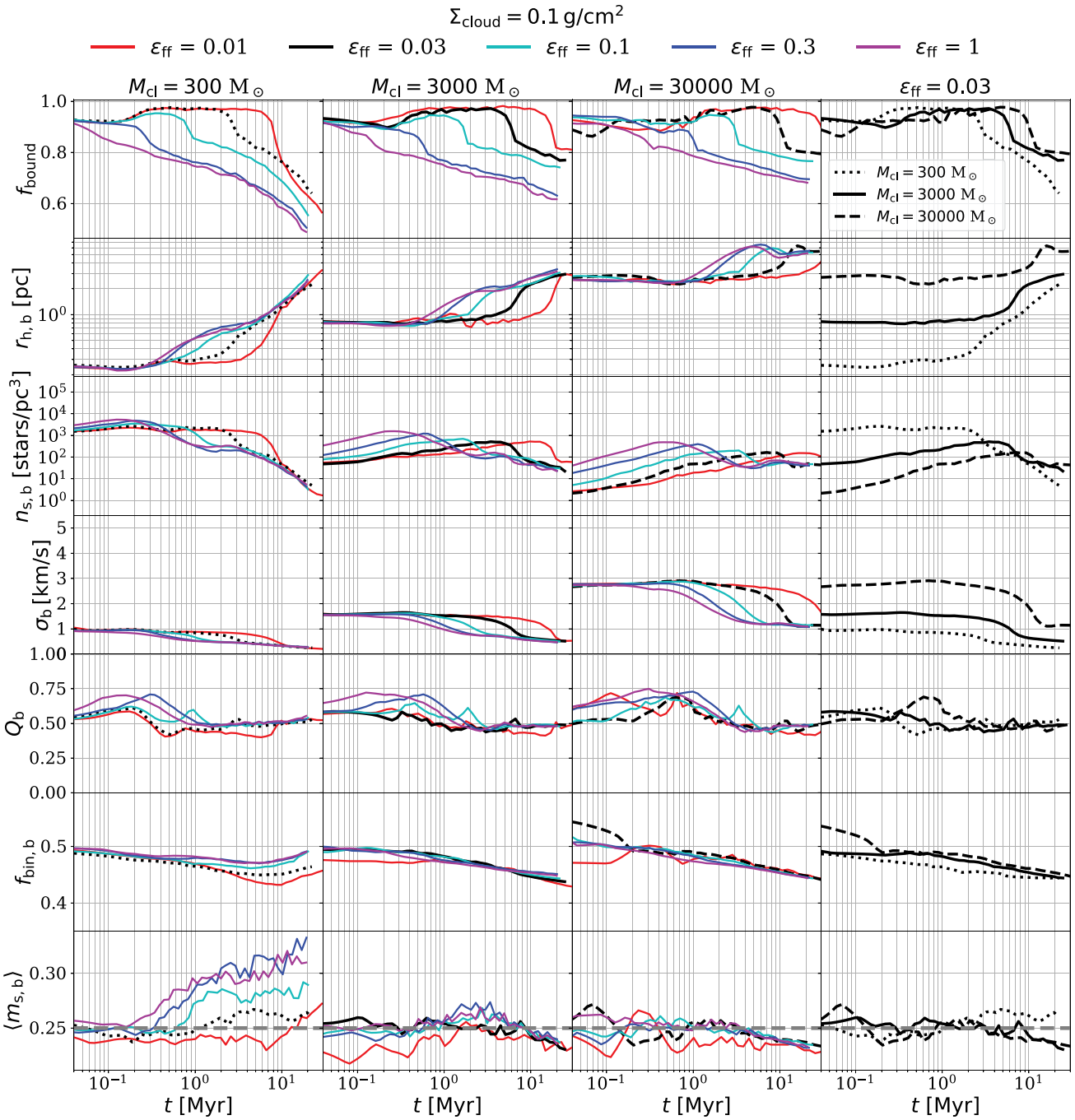

Figure 3. Time evolution of various properties of star clusters formed within a mass surface density environment of $\Sigma_{cloud} = 1.0\,g\,cm^{-2}$, global $\epsilon = 0.5$ and different values of ϵ_{ff} (see legend). The lines in each panel show median values calculated from all the simulations of each set. First, second, and third columns show the cases of $M_{cl} = 300$, 3000, and $30\,000\,M_\odot$, respectively, while the fourth column shows a comparison of all masses for the fiducial choice of $\epsilon_{ff} = 0.03$. Top row shows the fraction of bound mass in the cluster relative to the instantaneous total formed stellar mass. Second row shows the evolution of the half-mass radius $r_{h,b}$ for the bound stars. Third row shows the average number density of systems ($n_{s,b}$), i.e. singles and binaries, measured inside the volume defined by $r_{h,b}$. Fourth row shows the evolution of the velocity dispersion measured inside $r_{h,b}$. Fifth row shows the evolution of the virial ratio of the bound stellar component (Q_b). Sixth row shows the evolution of the bound binary fraction ($f_{bin,\,b}$). Bottom row shows the average system mass (singles and binaries) for stellar systems with primaries less massive than $7\,M_\odot$, where horizontal grey dashed line shows the expected average value given the input IMF.

environments. Dynamical relaxation drives subsequent expansion, but at a much slower rate than in the low-mass clusters. Again, the slow-forming models do not have a chance to enter the PFS phase. We note that by 20 Myr the clusters forming from $M_{cl} = 3000\,M_\odot$ clumps reach sizes of $r_{h,b} \sim 3$ pc, with this being quite insensitive to Σ_{cloud} and ϵ_{ff}, even though they can reach this size with quite different evolutionary histories, especially for the low-ϵ_{ff} and low-Σ_{cloud} cases.

The $M_{cl} = 30\,000\,M_\odot$, $\Sigma_{cloud} = 1\,g\,cm^{-2}$ case produces even more compact clusters with $r_{h,b} \sim 2$ pc at 20 Myr, independent of

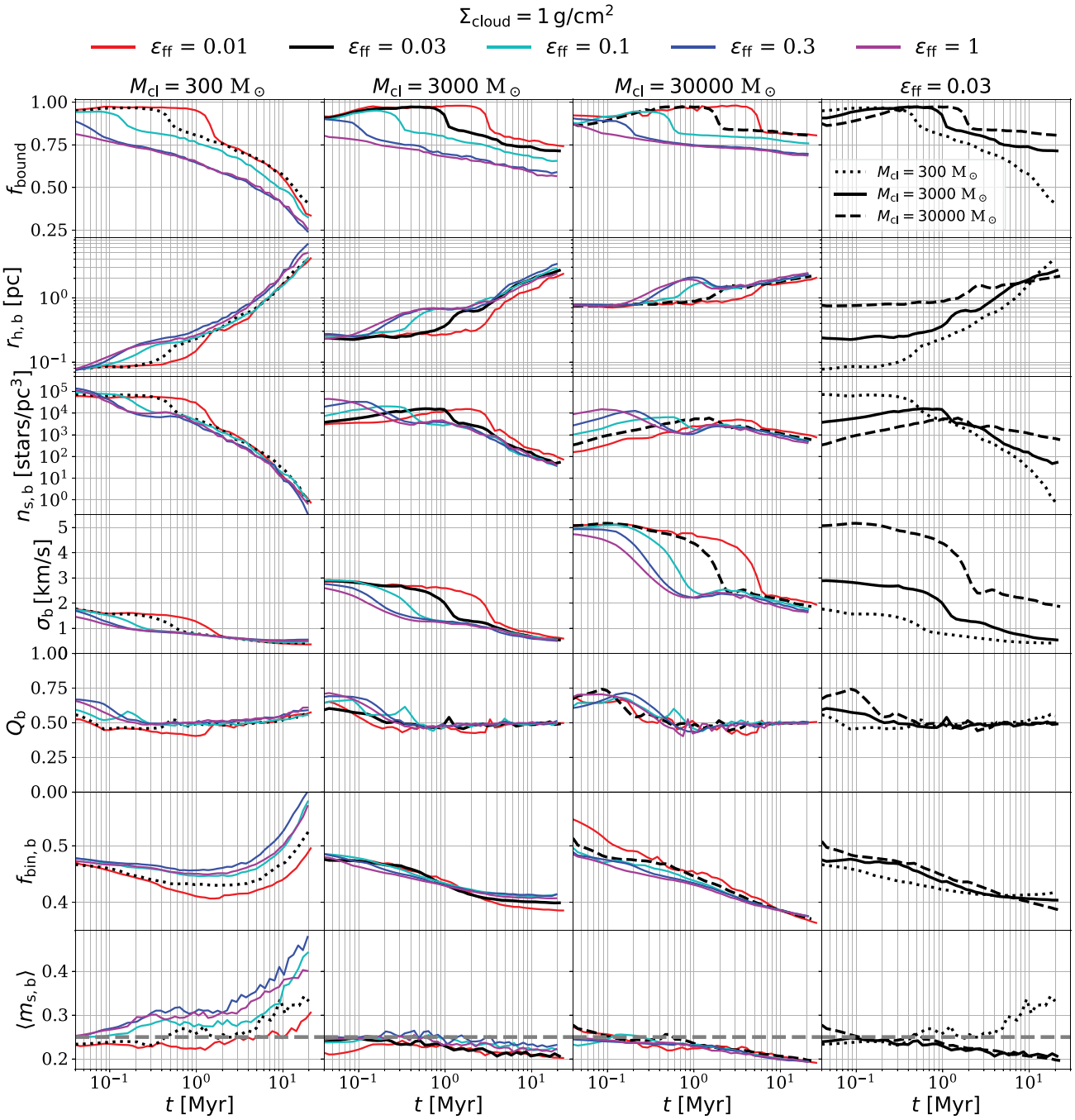

Figure 4. Same as Fig. 3, but for $\Sigma_{\rm cloud} = 1.0\,{\rm g\,cm^{-2}}$.

$\epsilon_{\rm ff}$. Again, the evolution to this state involves a phase in which the cluster expansion is essentially halted (even with a 'bounce' for $\epsilon_{\rm ff} \gtrsim 0.1$) at $r_{\rm h,b,PFS} \simeq 1.5$ pc within the first few Myr (depending on $\epsilon_{\rm ff}$), before the cluster relaxation expansion phase, which here occurs at a very slow rate compared to the lower mass clusters. In the $\Sigma_{\rm cloud} = 0.1\,{\rm g\,cm^{-2}}$ case, the massive clusters stop expanding at $r_{\rm h,b,PFS} \simeq 6$ pc (and with $n_{\rm s,b} \sim 100\,{\rm pc^{-3}}$), although the slowest forming model with $\epsilon_{\rm ff} = 0.01$ does not have time to reach this state within ~ 20 Myr. Furthermore, these massive, low-density clusters do not have time to exhibit significant expansion driven by dynamical relaxation during the duration of the simulations investigated here, i.e. up to ~ 20 Myr.

To more fully illustrate the evolution of cluster sizes, in Fig. 5 we show in the top rows of the top and bottom set of panels the time evolution of $r_{\rm h,b}$ normalized by the initial clump radius. We see that $r_{\rm h,b,\,PFS}$ is about a factor of 1.5 and 2 times larger than $R_{\rm cl}$ for the low- and high-$\Sigma_{\rm cloud}$ cases, respectively. Then, by about 20 Myr, clusters have typically been able to expand by factors of 2 (for large clusters with $M_{\rm cl} = 30\,000\,{\rm M_\odot}$) to 40 (for small clusters with $M_{\rm cl} = 300\,{\rm M_\odot}$) compared to the size of their natal gas clumps.

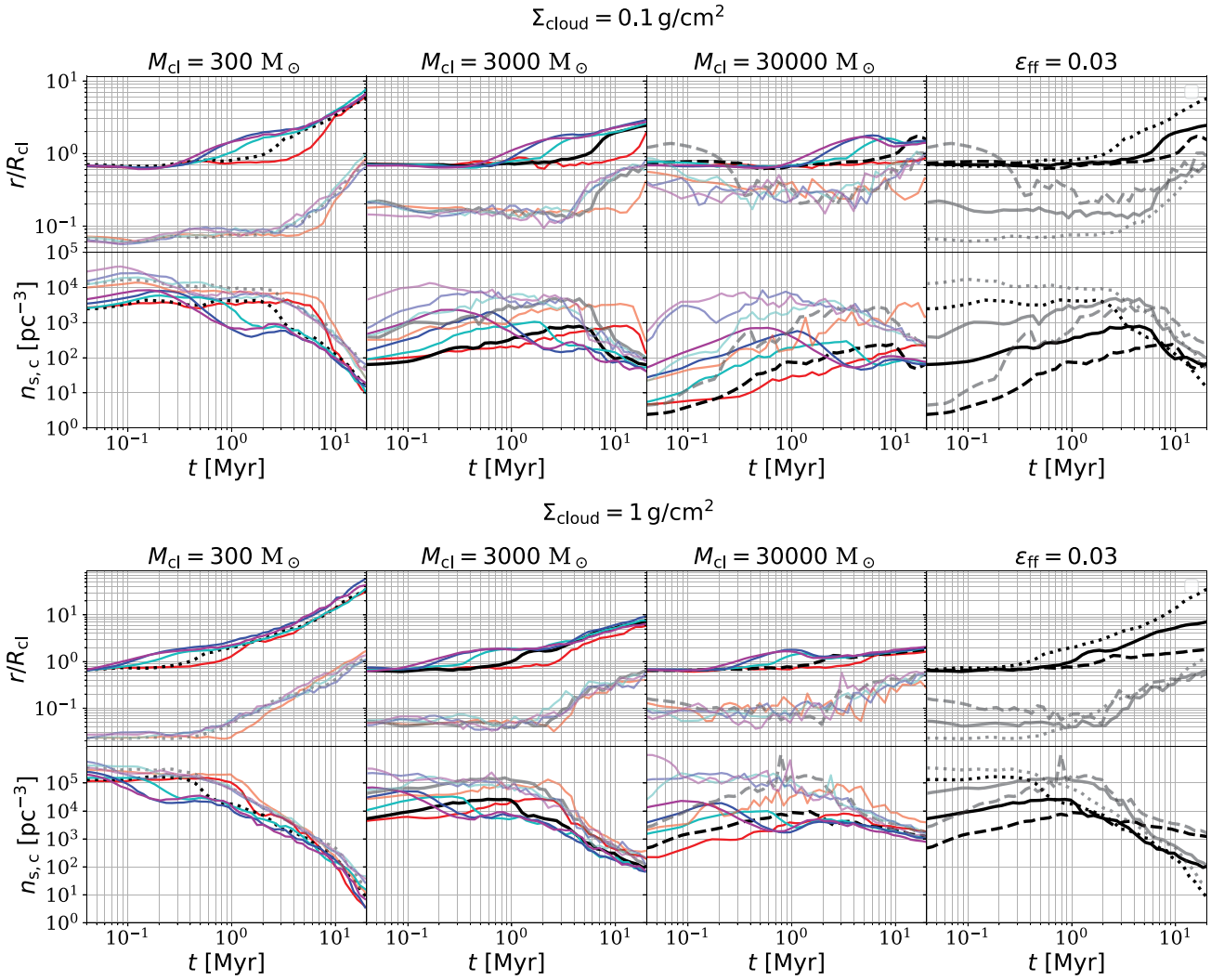

Figure 5. Evolution of average size and number density for all simulations in this work. Top and bottom set of panels shows simulations with $\Sigma_{\rm cloud} = 0.1\,{\rm g\,cm^{-2}}$ and $\Sigma_{\rm cloud} = 1.0\,{\rm g\,cm^{-2}}$, respectively. Different colours show the adopted $\epsilon_{\rm ff}$ with the same colour scheme as in Figs 3 and 4. The first three columns group simulations with the same $M_{\rm cl}$, while the fourth column compares models with different values of $M_{\rm cl}$ for the $\epsilon_{\rm ff} = 0.03$ case. Solid lines in the top rows show the evolution of the average bound half-mass radii, $r_{\rm h,b}$, normalized by the initial clump radius, $R_{\rm cl}$. Semitransparent lines show the respective normalized core radii. The bottom rows show the evolution of number densities within the bound half-mass radii, $n_{\rm s,b}$, and within the core radii, $n_{\rm s,c}$.

Another important radial scale is the cluster core radius, defined as the 'density'-weighted average distance of the stars from the density centre in the cluster, where the 'density' of each star is estimated using the mass in a sphere containing the six nearest neighbours (Casertano & Hut 1985; Aarseth 2003). The time evolution of the core radii, normalized by $R_{\rm cl}$, is also shown in Fig. 5. These cluster core radii are relatively constant during the formation phase and are systematically larger for the more massive clusters. In addition, we see that core radius evolution appears to be independent of $\epsilon_{\rm ff}$, with the exception of the $\epsilon_{\rm ff} = 0.01$ case. In all models, we see that the main expansion phase of the core radius begins at about the same time, i.e. after about one crossing time of the region. The PFS phase ends as part of this core radius expansion phase, i.e. the half-mass radius expands in step with the core radius. The case of $\epsilon_{\rm ff} = 0.01$ is different because the core radius is held in place by the background potential, delaying the expansion of the cluster and not going through a PFS phase since the core is already relaxed. We see that at about 20 Myr these cluster core radii, although still expanding, have evolved to be quite similar to the initial clump radii.

The third rows of Figs 3 and 4 show the time evolution of the average number densities of the stars inside $r_{\rm h,b}$. These respond accordingly to the evolution of $f_{\rm bound}$ and $r_{\rm h,b}$. In general, in our models, lower mass clusters form from denser clumps and so during the formation phase have higher number densities of stars than more massive clusters. However, given that they start expanding earlier, this situation reverses during the first few Myr. The slower forming clusters take longer to build up their stellar densities, but retain these levels for longer periods of time. We will see later that this affects their overall efficiency at producing runaway stars via dynamical ejections. However, we note that it is the number densities in the densest part of the clusters, i.e. in their cores, which are important for production of most close interactions leading to dynamical ejections. Thus, in Fig. 5 (bottom rows of each set of panels) we also show the time evolution of $n_{\rm s,c}$, i.e. the average number density of stellar systems within the core radius. We see that the number densities in

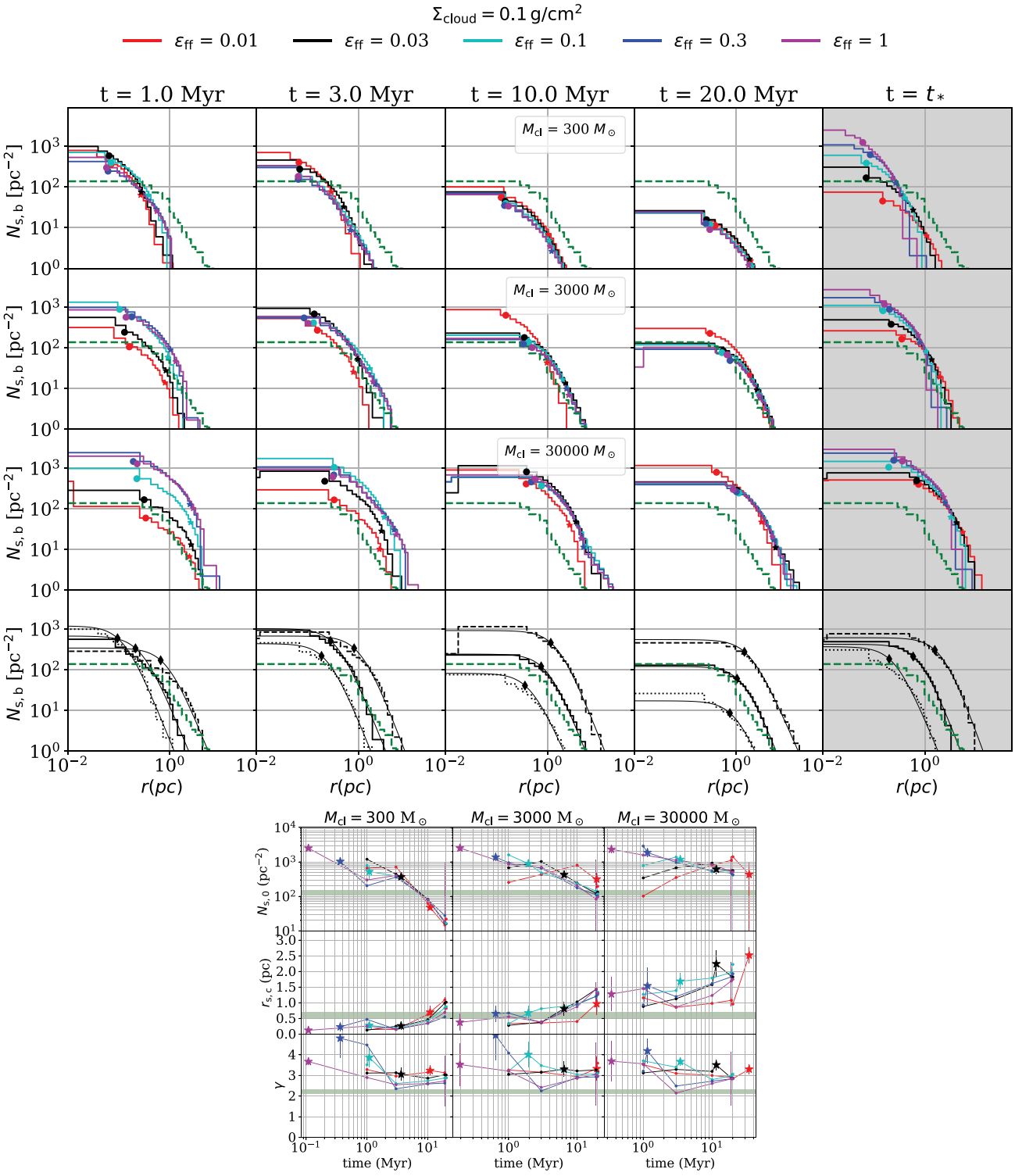

Figure 6. Top: Projected number density profiles for simulations with $\Sigma_{\rm cloud} = 0.1\,{\rm g\,cm^{-2}}$. Profiles are measured at $t = 1$, 3, 10, 20 Myr and when star formation is finished at $t = t_*$ (columns, left to right). Filled circle, diamond, and star symbols show the positions of the core radius ($r_{\rm c,b}$), fit scale radius ($r_{0,\rm b}$), and half-mass radius ($r_{\rm h,b}$), respectively. The first three rows present the cases for $M_{\rm cl} = 300$, 3000, and 30 000 $M_\odot$, i.e. to allow easy visualization of the effects of $\epsilon_{\rm ff}$. The fourth row compares the $\epsilon_{\rm ff} = 0.03$ cases for the different masses, with dotted, solid, and dashed histograms showing $M_{\rm cl} = 300$, 3000, and 30 000 $M_\odot$, respectively. Thin solid lines in the fourth row show the best fits of equation (11). Radial binning is constructed so that each bin has the same number of stars. Green dashed lines show the density profile of the ONC based on the membership list by Da Rio et al. (2016). Bottom: Time evolution of fitted structural parameters of equation (11), measured at the same times as in the above profiles. Star symbols show the results at $t = t_*$. Green horizontal bands show the values of these parameters that are estimated for the ONC from the data of Da Rio et al. (2016).

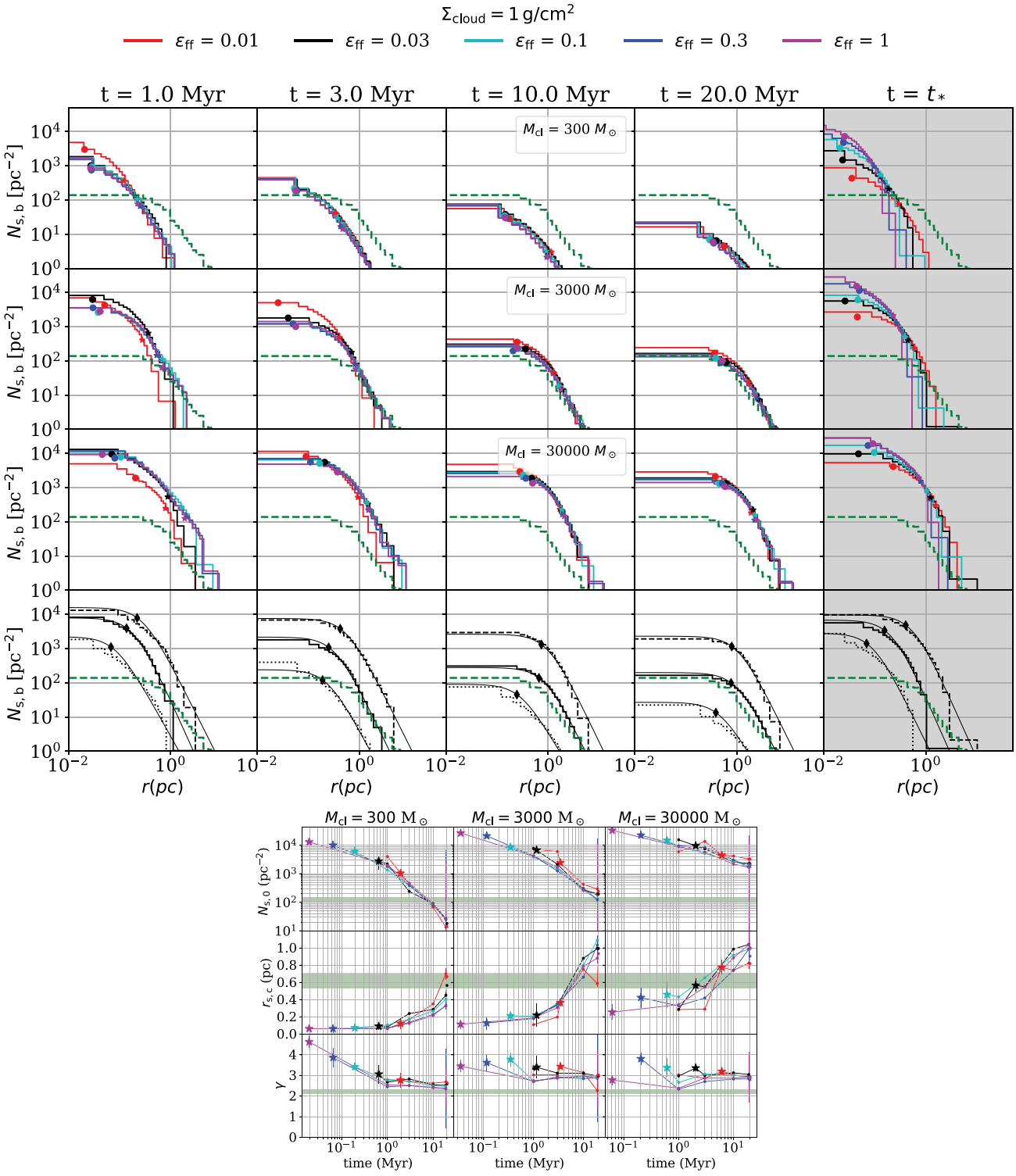

Figure 7. As Fig. 6, but for $\Sigma_{cloud} = 1.0\,g\,cm^{-2}$.

the core regions can be many times larger than that averaged over the half-mass scale, especially for the most massive clusters. Thus, in general, the full density profile of a cluster needs to be considered for estimation of quantities, such as interaction rates, that depend on local densities.

For the purposes of comparing to observed star clusters, where the true 3D structure is hard to measure, it is better to consider the projected surface number density profiles, i.e. $N_s(r)$, with this being the number of stellar systems (singles, binaries, and higher order multiples) per unit projected area. Figs 6 and 7 show these projected radial profiles of the bound clusters as they evolve during the simulations. These profiles are averages of all sets of the same model at a given time.

Our simulated clusters tend to have a similar radial structure. We characterize this using the model of Elson, Fall & Freeman (1987), which was developed to describe luminosity profiles of young star

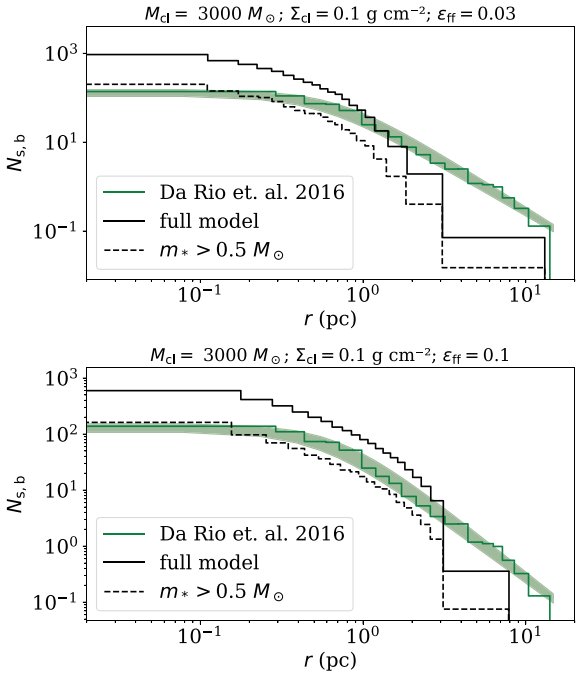

Figure 8. In each panel, the green line shows the ONC projected number density profile derived from the membership list provided by Da Rio et al. (2016). Green shaded area shows the range of best-fitting ONC profiles according to equation (11). The ONC data are compared to two of our models with $\Sigma_{\rm cloud} = 0.1\,{\rm g\,cm^{-2}}$ and $M_{\rm cl} = 3000\,{\rm M_\odot}$ measured at 3 Myr (black solid lines). Top panel compares to our fiducial model with $\epsilon_{\rm ff} = 0.03$, and bottom panel to a model with $\epsilon_{\rm ff} = 0.1$. Dashed lines show the same modelled profiles, but excluding stars with masses below $0.5\,{\rm M_\odot}$, which is a simple way to illustrate the effects of potential incompleteness.

clusters. Then, the surface number density profiles are described via:

$$N_{\rm s}(r) = N_{\rm s,0}\left(1 + \frac{r^2}{r_{\rm s,0}^2}\right)^{\gamma/2}, \tag{11}$$

where $N_{\rm s,0}$ is the central surface number density, $r_{\rm s,0}$ is a scale radius, and γ is a power-law exponent. The best-fitting parameters at each measured time are shown in the lower set of panels in Figs 6 and 7. Equation (11) typically provides a good description for the models presented here. At early stages most models have steep power-law haloes, but as star clusters relax they tend to converge to a shallower distribution with $\gamma \simeq 2.5$ for the low-mass clusters and $\simeq 3$ for the more massive ones. The scale radius tends to be between the core and half-mass radii.

As an example comparison with an observed young star cluster, we have constructed the number density profile of the Orion Nebula Cluster (ONC) based on the membership list compilation provided by Da Rio et al. (2016). We have selected stars flagged as members by any of the methods described by Da Rio et al., working within a 2 deg radius around the ONC, which yields a total of 1464 sources. We have transformed the coordinates of the stars to parsecs using an ONC distance of 403 pc (Kuhn et al. 2019) and constructed the projected number density profile using 20 bins, each with approximately equal number of stars. The obtained best-fitting parameters of equation (11) to these data are

$$\begin{aligned} N_{\rm s,0} &= 132 \pm 22\ {\rm pc^{-2}}, \\ r_{\rm s,0} &= 0.62 \pm 0.09\ {\rm pc}, \\ \gamma &= 2.2 \pm 0.1. \end{aligned} \tag{12}$$

We show the profile defined by these values with the green dashed lines and green shaded areas in Figs 6 and 7, as well as in Fig. 8.

While our numerical models have not been specifically tailored to the ONC properties, we see that our derived the fitting parameters, especially of the low-$\Sigma_{\rm cloud}$ cases, are typically quite similar to those shown by the ONC in its current state. For instance, at the age of the ONC (i.e. $\sim$3 Myr), the closest models to the ONC in terms of total mass are clusters with $M_{\rm cl} = 3000\,{\rm M_\odot}$. At $\sim$3 Myr, the low-density clusters reproduce the measured scale radius $r_{\rm s,c}$. However, the ONC's central density, $N_{\rm s,0}$, is rather low in comparison with our models. One potential mitigating factor is that the observational sample of Da Rio et al. (2016) is incomplete in the brown dwarf regime and its incompleteness may be relatively higher in the central regions due to effects of higher extinction, nebulosity and crowding compared to outer regions. Fig. 8 shows more detailed comparisons of some of our model clusters, including the effects of incompleteness below $0.5\,{\rm M_\odot}$, with the observed surface number density profile of the ONC. We see here that the ONC has a relatively shallower outer projected density distribution, i.e. with $\gamma = 2.2$, compared to our simulated clusters, i.e. with $\gamma = 2.5$. While this could be a real physical discrepancy, i.e. indicating a limitation of the model, it could also be caused by contamination by false-positive members in the outskirts of the ONC.

In summary, we see that our modelled star clusters develop a surface density profile that is quite similar to that exhibited by the ONC. However, further work on simulated clusters that are more specifically tailored to this and other observed clusters, including effects of observational incompleteness, are needed before one would be able to constrain model parameters of $M_{\rm cl}$, $\Sigma_{\rm cloud}$, and $\epsilon_{\rm ff}$.

4.2 Evolution of kinematics and dynamics

The fourth rows of Figs 3 and 4 show the time evolution of the 1D velocity dispersions of the bound members of the clusters, $\sigma_{\rm b}$. The clusters start with velocity dispersions given by their parental gas clumps (see Table 1). At first, during the formation phase, these remain relatively constant, although in the high-$\Sigma_{\rm cloud}$ cases $\sigma_{\rm b}$ declines slowly even during this phase. Following the formation phase, the velocity dispersions decline at a faster rate as the clusters expand and lose mass from the bound component. By $\sim$20 Myr some clusters, e.g. the most massive clusters forming from low-density environments, have a chance to reach a relatively stable level of $\sigma_{\rm b}$, just larger than $1\,{\rm km\,s^{-1}}$.

The fifth rows of Figs 3 and 4 show the evolution of the virial ratio of the bound stellar system defined, in its most general form as

$$Q_{\rm b} \equiv \frac{E_{\rm kin,b}}{E_{\rm grav,b}}, \tag{13}$$

where $E_{\rm kin,b}$ is the total kinetic energy of the bound stars and $E_{\rm grav,b} = \sum_{i=1}^{N_{\rm b}} \boldsymbol{F_i} \cdot \boldsymbol{r_i}$ is the gravitational energy of the bound stars. In this calculation, binaries are treated as single unresolved systems.

A cluster in virial equilibrium has $Q_{\rm b} = 0.5$. As introduced in previous papers in this series, the star clusters formed in our framework do so from an initially supervirial state since the natal

clump has a significant surface pressure applied to it from its surroundings. For all simulations in this paper, the initial global $Q \approx 1$. As the stellar systems relax from their initial configurations, they will achieve approximate equilibrium on a time-scale of the order of one relaxation time, $t_{\rm relax} \simeq (N/\ln N)t_{\rm cr}$.

As seen in Paper II, the ratio of the time-scale over which Q relaxes into equilibrium, $t_{\rm relax}$, compared to the formation time, t_*, is important because by the end of formation, when the background gas is exhausted, the different $\epsilon_{\rm ff}$ models can then start their gas-free stage from different dynamical states. For example, a star cluster that forms quickly (e.g. $\epsilon_{\rm ff} = 1$) does not have time to relax and is still supervirial by the time gas is exhausted. On the other hand, a star cluster that forms slowly ($\epsilon_{\rm ff} = 0.01$) has enough time to relax and starts its gas free evolution closer to virial equilibrium.

Figs 3 and 4 show that this trend persists at different clump masses. In general, the crossing time (and thus also the relaxation time) in the formation phase is shorter than after gas is gone. Then, slow-forming models are able to relax even earlier than fast forming models that already lost their gas mass at supervirial states. Thus, slow-forming star clusters are able to be already near virial equilibrium long before star cluster formation is finished.

4.3 Evolution of binary properties

The sixth rows of Figs 3 and 4 show the evolution of the binary fractions in the bound clusters, $f_{\rm bin,b}$. Note that the stars are formed, statistically, with an average binary fraction of 0.5. There is a gradual decline seen due to disruption of binaries, which can occur via dynamical interactions and also as a result of stellar evolution, i.e. supernova explosions. The evolution of the binary fraction shows significant differences depending on $M_{\rm cl}$, $\Sigma_{\rm cloud}$, and $\epsilon_{\rm ff}$. Small clusters of $M_{\rm cl} = 300\,{\rm M}_\odot$ quickly process binaries during their formation phase, especially at low $\epsilon_{\rm ff} = 0.01$ where $f_{\rm bin,b}$ reaches a minimum of 0.4 in the high-$\Sigma_{\rm cloud}$ case. This minimum is quite sensitive to $\epsilon_{\rm ff}$, given the longer formation time compared to the local crossing time of the regions. After reaching this minimum, a few Myr after the start of formation, there then follows a significant increase in $f_{\rm bin,b}$.

In Fig. 9, we present a more detailed exploration of the evolution of the binary fraction, separating those for the bound (grey panels) and unbound (white panels) populations. The rise in $f_{\rm bin}$ at late times in the low-mass simulations mostly happens within the bound clusters and is caused by the creation of new 'dynamically formed' binaries. The fifth and sixth rows in this figure show the fraction of dynamically formed binaries in the bound and unbound populations, respectively. These dynamically formed binaries include those that were primordial but later exchanged one of their members with other binaries or singles stars. We see that in the low-mass simulations by 20 Myr about ∼6–8 per cent of binaries in the bound cluster are formed dynamically, while it is about half of this level (∼ 3–4 per cent) in the unbound population.

In the higher $M_{\rm cl}$ cases, we see that the binary fractions in the bound clusters decrease to lower values, e.g. reaching close to 0.3 after about 20 Myr in the $M_{\rm cl} = 30\,000\,{\rm M}_\odot$, $\Sigma_{\rm cloud} = 1.0\,{\rm g\,cm^{-2}}$ case. This is caused by there being more time for disruption of binaries by close encounters with other stars in these clusters, which retain a high bound fraction over this period. These clusters also have a smaller fraction of dynamically formed binaries, which is not enough to change the global binary fractions, unlike in the lower mass cases.

4.3.1 Binary population

Here, we examine how the binary population is processed in the different models. We have seen in Paper I and Paper II that there was relatively little processing of the primordial binary population. However, we have also seen from Fig. 4 that in the clusters presented in this paper there is a significant reduction in the fraction of binaries by 20 Myr in the most massive, high-density model: about a third of the initial binaries have been disrupted in this case. This change appears to be driven by dynamical processing, rather than as a consequence of stellar evolution.

We examine the properties of the populations of binaries, both the ones that have been disrupted and the ones formed later during the evolution of the cluster. We note that we have also looked for higher order multiples in the models (as defined by the NBODY6++ code), however these are found to form in negligible numbers, of the order of 1 per simulation in most models and a maximum typical number of 4 in the `m30000H` models. Such small number of multiples is expected given that our initial conditions did not include them, and we see that forming stable multiples by capture is a rare event in these models.

In Fig. 10, for simulations with $\epsilon_{\rm ff} = 0.03$ we show the average fraction of binaries that are disrupted at different times in the evolution, i.e. from left-hand column to right-hand, at $t = 1$, 3, 10, 20 Myr and at $t = t_*$, with $M_{\rm cl} = 300\,{\rm M}_\odot$ in red, $3000\,{\rm M}_\odot$ in black, and $30\,000\,{\rm M}_\odot$ in blue, and with low- and high-$\Sigma_{\rm cloud}$ cases with solid and dashed lines, respectively. The first row shows the fraction of disrupted binaries as a function of initial primary mass. We see that at early times the mass of the primary star has little influence on binary disruption. However, by 10 Myr the disrupted fraction has risen for more massive stars, which is due to stellar evolution, especially core-collapse supernovae to neutron stars that then receive high kick velocities.

The second row of panels in Fig. 10 shows the disrupted fraction of binaries as a function of initial semimajor axis (a). The typical semimajor axis in our models is around 20 au. Below this value, most binaries survive across the models, which is expected since these are relatively hard binaries. Wider binaries (i.e. with $a \gtrsim 100$ au) are the most affected, with disruption fractions that depend sensitively on the environment, e.g. between 10 and 80 per cent of binaries with $a \sim 1000$ au are disrupted depending on the model, where the main factor is the density of the environment as parametrized by $\Sigma_{\rm cloud}$. For the range above 100 au, the disruption fractions are clearly defined by density and parent clump mass. The most massive clusters show lower disruption fractions within the same $\Sigma_{\rm cloud}$, since these clusters have lower initial number densities (see Section 2.2). In general, low $\epsilon_{\rm ff}$ results in a larger disruption fraction, with $\epsilon_{\rm ff}$ having a larger effect on low- and medium-mass models (see Appendix A), with a variation of 25–40 per cent at $a = 1000$ au. In the high-mass clusters with $M_{\rm cl} = 30\,000\,{\rm M}_\odot$, variations in disruption fractions are less than 5 per cent between different $\epsilon_{\rm ff}$ cases. Most binary disruption happens early in the evolution, so that by 1 Myr most of these features are already set.

We also explore the details of the dynamically formed binaries in the clusters. As shown in Fig. 9, up to 7 per cent of binaries in clusters with $M_{\rm cl} = 300\,{\rm M}_\odot$ are formed dynamically, where most of these binaries are part of the bound cluster component. The third row of Fig. 10 shows the fraction of binaries that are dynamically formed as a function of primary initial mass. A clear trend appears where the more massive stars tend to capture other stars more efficiently. This trend is strongest in the lowest mass clusters, which undergo the highest degree of dynamical processing, and the fact in these

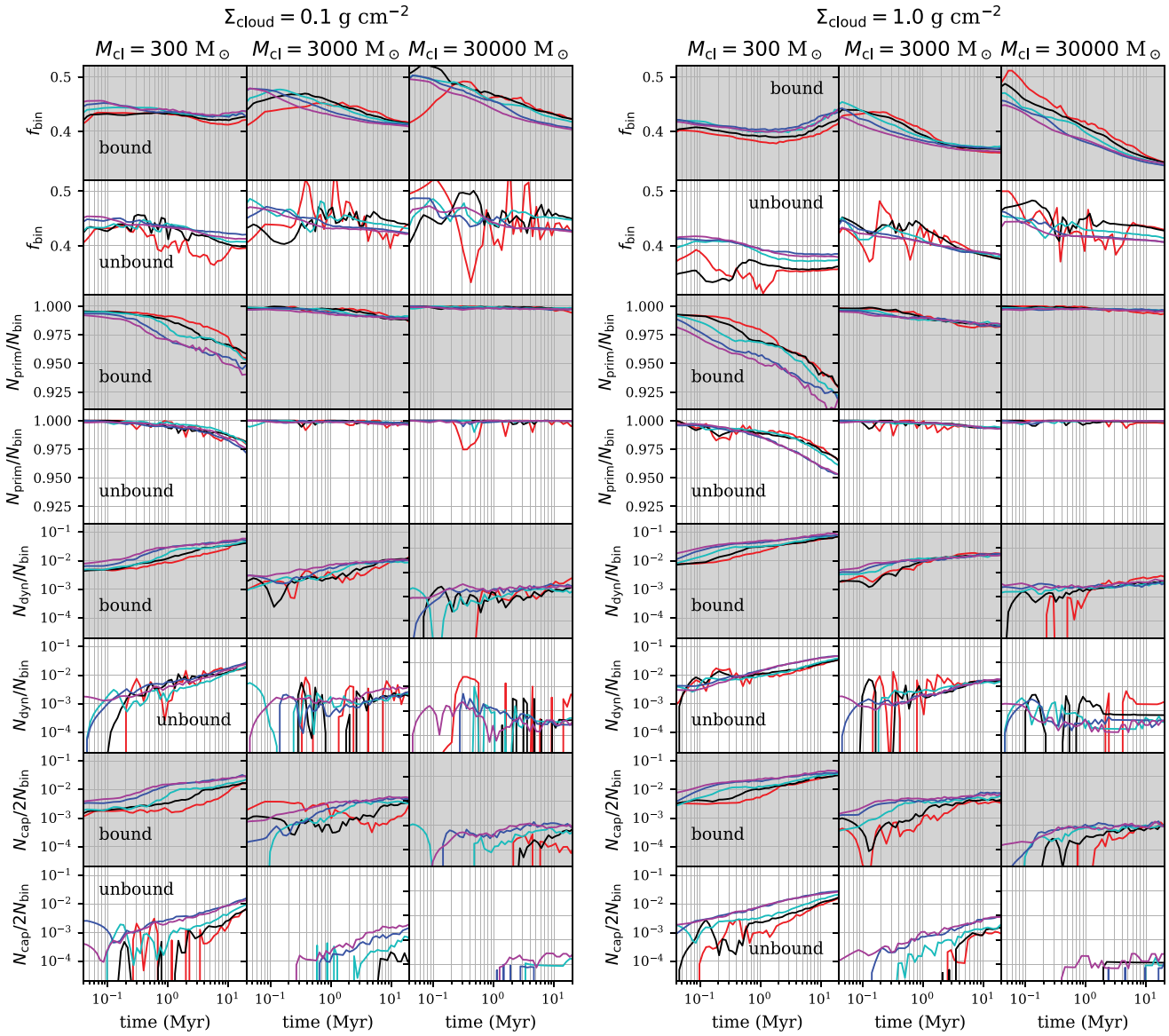

Figure 9. Detailed evolution of binary properties, shown separately from the bound (grey background panels) and unbound (white background panels) populations of stars, for simulations with $\Sigma_{\rm cloud} = 0.1\,{\rm g\,cm^{-2}}$ (left) and $1.0\,{\rm g\,cm^{-2}}$ (right). Colour scheme of the lines is the same as in previous figures denoting the adopted $\epsilon_{\rm ff}$. From top to bottom, the first two rows show the binary fraction ($f_{\rm bin}$) of the bound and unbound populations. The third and fourth rows show the fraction of binaries that are primordial, i.e. $N_{\rm prim}/N_{\rm bin}$, where $N_{\rm prim}$ and $N_{\rm bin}$ are the number of primordial and total number of binaries, respectively. The fifth and sixth rows show the fraction of binaries formed dynamically, with $N_{\rm dyn}$ as their total number. The seventh and eighth rows show the fraction of binary members that were originally single stars, i.e. the number of captured singles $N_{\rm cap}$ divided by the total number of binary members, i.e. $2N_{\rm bin}$.

low-mass clusters, A-, F-, and even G-type stars, can be the most massive stars in the cluster, and be the ones segregating to the centre. Furthermore, since the overall velocity dispersion is lower, then gravitational focusing is favoured for less massive stars in these environments. Again, the $\epsilon_{\rm ff}$ parameters appear to play only a minor role in the formation of binaries, as can be seen in the formation fractions at 20 Myr for other $\epsilon_{\rm ff}$ (see Appendix A). Most of the dynamically formed binaries are wide binaries with semimajor axes larger than 1000 au, as can be seen in the fourth row of panels in Fig. 10. Here, we can also see that higher primordial density favours the formation of tighter binaries, since harder binaries are able to be perturbed allowing interchange of their members.

Note that the results shown in the first to fourth rows in Fig. 10 are fraction of binaries in each bin. The most affected types of binaries, i.e. the wider and more massive ones, are in fact the less populated parts of the binary distribution, representing only a small fraction of the total number of binaries in the system. In the fifth row of Fig. 10, we show the full distribution of binaries as a function of semimajor axis as an average per simulation. Then after all stars are formed, the average numbers in the `m30000` case is 10 times larger than in the `m3000` case and 100 times than in the `m300` case. We see that in the `m3000` and `m30000` models, dynamical disruption of binaries causes a steeper decrease of frequency for binaries with large a, where the fractional decrease is shown in the second row of panels. However, for `m300` the dynamical formation of binaries is considerable ($\sim$7 per cent) and concentrated in the high end of the distributions ($a > 1000$ au), producing a second peak at $a \sim 10^5$ au, with the strength of this peak being higher for the larger $\Sigma_{\rm cloud}$ case.

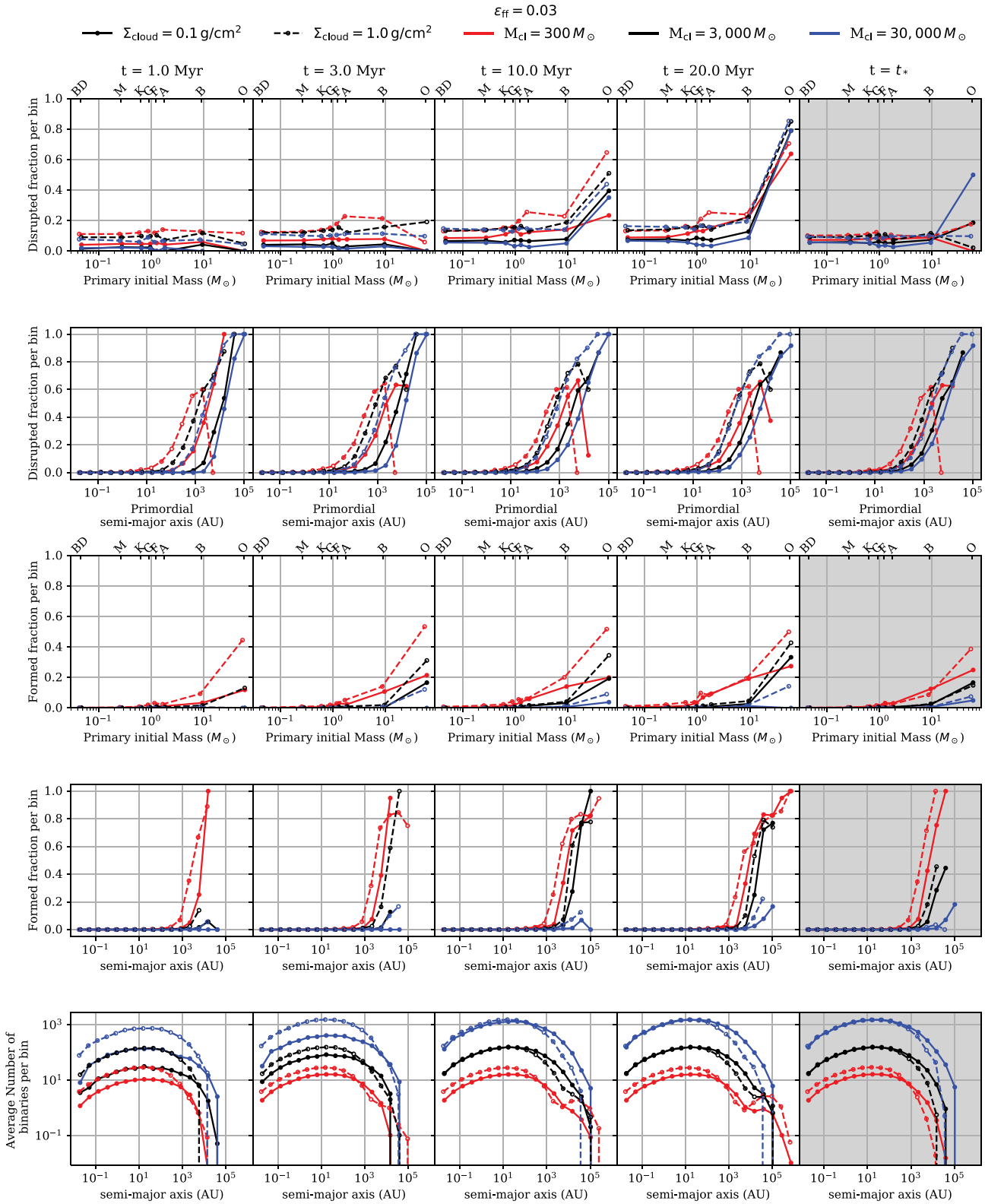

Figure 10. Distribution of primary mass and semimajor axis for different kinds of binaries, measured at (from left-hand to right-hand columns) $t = 1$, 3, 10, 20 Myr and when star formation stops (t_*). This figure shows the results for simulations with $\epsilon_{ff} = 0.03$ and $M_{cl} = 300$ (red), 3000 (black), and 30 000 $M_\odot$ (blue), and for simulations with $\Sigma_{cloud} = 0.1$ (solid lines) and 1.0 g cm^{-2} (dashed lines). First and second rows show the fraction of disrupted primordial binaries per primary stellar type (first row) and primordial semimajor axis bin (second row). Third and fourth rows show the fraction of binaries that are formed dynamically separated by stellar type (third row) and current semimajor axis. Fifth row shows the total distribution of semimajor axes averaged by simulation set.

4.4 Evolution of the stellar mass function

The stellar mass function (MF) is expected to evolve within the clusters due to a combination of mass segregation, binary formation/disruption, ejection of walkaway/runaway stars, and stellar evolution. The bottom rows of Figs 3 and 4 show the average system mass, i.e. single stars, binaries, and higher order multiples (although the latter are negligible), in the bound cluster populations for systems with primary masses below 7 $M_\odot$ (i.e. so that these are not significantly affected by stellar evolution during the period considered). For the assumed IMF and binary sampling methods, this average system mass has an expected value of 0.25 $M_\odot$, shown by a horizontal grey dashed line in each of the panels.

As the clusters evolve, we see that small clusters show the largest deviation from the expected value. Models `m300` show a remarkable variation in the average system mass, i.e. rising by a factor of $\gtrsim$1.6 in the high-$\Sigma_{\rm cloud}$ cases with $\epsilon_{\rm ff} \gtrsim 0.1$. This dramatic change is related to the fact that these clusters evolve to have the smallest bound mass fractions, i.e. $f_{\rm bound} \sim 0.3$ and undergo the most significant dynamical processing, including significant formation of new binaries (see Section 4.3). The variations in average system mass are more modest in the `m3000` and `m30000` models and move in the opposite direction, i.e. decreasing to lower values. We attribute this behaviour to the fact that these clusters retain high bound mass fraction and tend to destroy their primordial binaries without forming significant numbers of new binaries.

Next, we examine signatures of mass segregation by considering the evolution of the MF slopes in the mass range above ∼1 $M_\odot$. We measure the stellar MF at different stages during the evolution of the modelled clusters, using only the bound stars and excluding neutron stars and black holes. Fig. 11 shows the resulting MFs when measured for stars within different Lagrangian radii at different times for our fiducial models with $\epsilon_{\rm ff} = 0.03$. However, comparison between the models is complicated by the large differences in formation and dynamical time-scales for these clusters that have orders of magnitude differences in mass and density. For instance, stellar evolution plays a different role in each case when the formation and relaxation times are comparable to the stellar evolution time-scales of the most massive stars. Effects due to ejection events derived from stellar evolution, i.e. velocity kicks of neutron stars or binary breaking, are especially important.

In Fig. 11, we first show the MFs at the end of the formation stage ($t = t_*$), when all stars have formed and the clusters start their gas-free phase. We pay special attention to the evolution of the high-mass end of the stellar MF, i.e. the range between 0.5 and 100 $M_\odot$, which by construction we have modelled with a canonical initial index of $\alpha_2 = 2.3$ (Kroupa 2001). We have performed linear fits to this range in logarithmic space as can be seen in Fig. 11 as solid lines within the fitting range. The fourth panel of the bottom row shows a comparison between the different α_2 values obtained at the different radii, $M_{\rm cl}$ and $\Sigma_{\rm cloud}$ for the case of $\epsilon_{\rm ff} = 0.03$. The same procedure was performed at 3, 10, and 20 Myr, where the corresponding fits are shown in the first three panels of the bottom row.

From the values of α_2 as a function of enclosing Lagrangian radius, we see that, by the end of star formation (fourth panel), the MFs tend to be more top heavy in the central regions of the cluster. However, in the `m30000L` model, which has t_* of 11.5 Myr, the population is already affected significantly by stellar evolution at this time (these clusters contain ∼25 stars more massive than 10 $M_\odot$).

At 3 Myr, top heavy MF signatures are most pronounced for the lowest mass clusters and the higher $\Sigma_{\rm cloud}$ cases, which, as discussed, have shorter relaxation times and thus shorter mass segregation times. Note that the low-$\Sigma_{\rm cloud}$ cases are all still forming stars at 3 Myr. In particular, the `m30000L` model is at about 25 per cent of its t_* and has not yet developed significant mass segregation. Similarly, the `m3000L` model is at about ∼50 per cent of t_* at this time and also does not show strong mass segregation.

When we consider the MFs at 10 and 20 Myr we see that mass segregation signatures are maintained and that even though stellar evolution mass-loss removes some of the excess of massive stars in the centre, enough intermediate massive stars sink here to keep the signatures present. In particular, the `m3000L` model has developed the strongest top heavy feature at 20 Myr. Therefore, we see that in all models, the central regions of the bound systems tend to become top heavy ($\alpha_2 < \alpha_{2,i}$), rather than bottom heavy, regardless of stellar evolution mass-loss.

Fig. 12 shows the evolution of the α_2 parameter for all models in this work measured at 10, 50, and 90 per cent Lagrangian radius, i.e. $\alpha_{2,10}$, $\alpha_{2,50}$, and $\alpha_{2,90}$, respectively. The signature of mass segregation can be more clearly seen when analysing the 10 per cent mass radius (top row of panels in each set).

The evolution of the $\alpha_{2,10}$ parameter is stronger in the `m300` models since their crossing times are shorter. Also, due to IMF sampling in small stellar clusters, the initial value of $\alpha_{2,10}$ is typically relatively high. As massive stars migrate to the centre, $\alpha_{2,10}$ decreases quickly. The maximum level of mass segregation is reached at the point when the core radii begin to expand, which does not happen at the end of star formation, but after about one initial crossing time regardless of $\epsilon_{\rm ff}$ (see Section 4.1). The $\alpha_{2,10}$ parameter then stabilizes at the onset of rapid expansion of the cluster core. Nevertheless, the central region MFs tend to remain top heavy compared to the IMF. Note that eventually, at later stages, $\alpha_{2,10}$ begins to increase due to the effects of stellar evolution.

4.5 High-velocity population

One important question we have explored during this series of papers is how the star cluster formation process is linked to the properties of the unbound/ejected population. We have shown in Paper II that slowly forming star clusters tend to produce more high-mass runaway stars. However, these models have so far only been for a single mass case of formation from a 3000 $M_\odot$ clump. Here, we examine how the high-velocity distribution changes with mass and $\epsilon_{\rm ff}$ in the framework of our models. We expect the results to be useful for interpreting data of runaways from young clusters, with a first application made for the 3000 $M_\odot$ models to the case of the ONC by Farias, Tan & Eyer (2020).

Fig.13(a) shows the 2D (plane of sky) velocity distribution for the low-$\Sigma_{\rm cloud}$ (left-hand column) and high-$\Sigma_{\rm cloud}$ (right-hand column) cases. Distributions are constructed at the time when star formation stops (t_*). The population of dynamically ejected stars manifests itself as an excess of high-velocity stars relative to the expected Maxwell–Boltzmann distribution for the given velocity dispersion. The initial expected velocity distribution, given the velocity dispersion of the natal gas clump, is shown as shaded areas in each panel. As time advances and gas is ejected, we have seen that the clusters expand and lower their velocity dispersion. However, the fastest formation models do not have time to relax and at $t = t_*$ their velocity dispersion is very similar to the one at birth. The resulting high-velocity excess at $t = t_*$ can be clearly seen, where the slowest forming clusters show a more evolved velocity distribution, with a lower velocity dispersion and greater fraction of high-velocity stars. However, since each cluster has a very different t_* it is difficult to

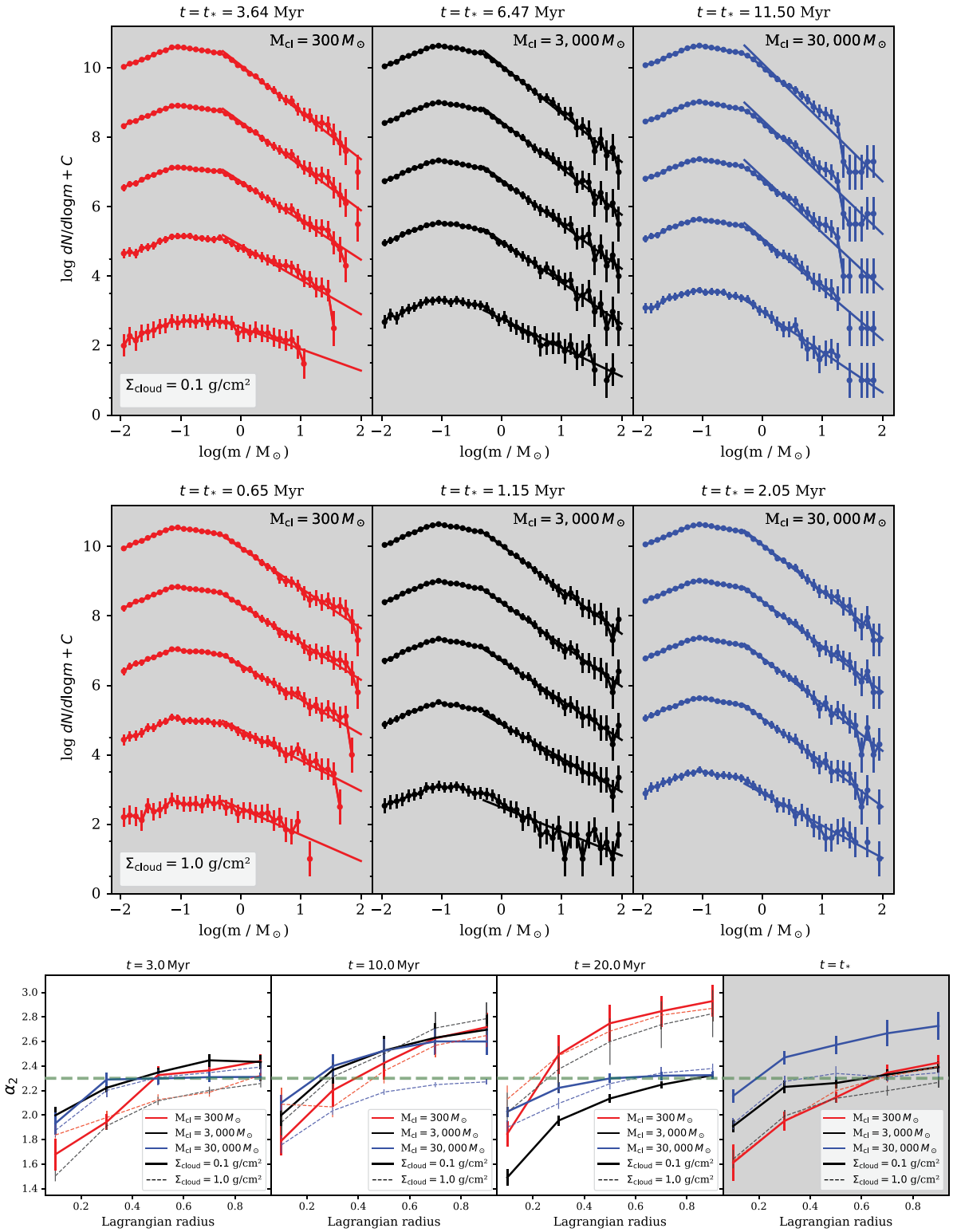

Figure 11. Mass functions measured at different Lagrangian radii and times for star clusters with $M_{\rm cl} = 300\,{\rm M}_\odot$ (red), $3000\,{\rm M}_\odot$ (black), and $30\,000 M_{\rm cl}$ (blue). First and second rows show the MFs measured at the end of star formation (t_*). The different MFs in each panel are measured within 0.1, 0.3, 0.5, 0.7, and 0.9 Lagrangian radii (from bottom to top). Bottom row shows linear fits to the range between 0.5 and $100\,{\rm M}_\odot$measured at $t = 3$, 10, 20 Myr and at $t = t_*$. The horizontal green dashed line shows the input value of $\alpha_2 = 2.3$ from Kroupa (2001).

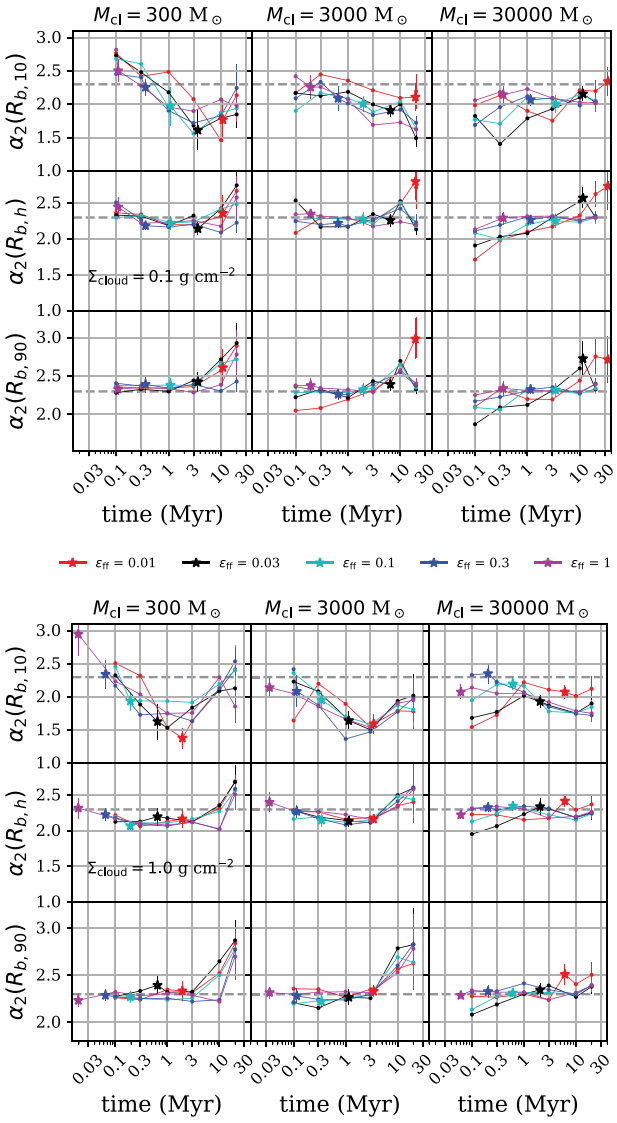

Figure 12. Evolution of α_2, i.e. the fitted mass function power-law parameter for the mass range between 0.5 and 100 M$_\odot$. Top and bottom sets of panels show the results for the low- and high-Σ_{cloud} cases, respectively, with different initial M_{cl} cases shown in the three columns. The top row in each set shows $\alpha_{2,10}$, i.e. the α_2 parameter measured within 10 per cent mass radius. Middle and bottom rows show the same parameter measured at the 50 per cent ($\alpha_{2,50}$) and 90 per cent ($\alpha_{2,90}$) mass radius, respectively, The colour scheme of the lines and points is the same as in previous figures representing the various ϵ_{ff} cases. Grey dashed line in each panel shows the input mass function in this range of $\alpha_2 = 2.3$. Star symbols mark the moment when star formation is finished and background gas is exhausted.

make a fair comparison between the models since we need to measure at different points in the evolution. Below, we develop a simple model to describe the evolution of the velocity distributions.

4.5.1 Velocity distribution model

Following our analysis in Paper I and Paper II, we note that our modelled star clusters are composed of three kinematically distinct components: (1) bound stars, which are those with a negative total energy; (2) unbound gently ejected stars, i.e. those that find themselves unbound given the rapid change in the protocluster potential; and (3) dynamically ejected stars, which are those that are ejected as a result of strong dynamical interactions. These groups have distinct velocity distributions that together compose the total velocity distribution shown in Fig. 13(a). The bound component can be described with a cumulative 2D Maxwell–Boltzmann velocity distribution function

$$\mathrm{CDF}(v, a) = 1 - \exp\left(-\frac{v^2}{2a^2}\right), \tag{14}$$

with the scale parameter given by

$$a = \sqrt{\frac{2}{4-\pi}}\sigma_b. \tag{15}$$

Note that for practical purposes, given the we are most interested in the high-velocity tail of the distribution where the numbers of stars are low, we instead use the survival function $\mathrm{SF}(v, a) = 1 - \mathrm{CDF}(v, a)$, which is the function shown in Fig. 13(a). The gently ejected component can be modelled with the same distribution, but with a larger velocity dispersion, which is a remnant of the dynamical history of the cloud. Therefore, the bound and unbound components are both described by an SF of the form:

$$\mathrm{SF}(v, a) = \exp\left(-\frac{v^2}{2a^2}\right). \tag{16}$$

The dynamically ejected stars follow a different distribution, i.e. approximately a power-law tail in the velocity distribution profile with an exponent γ. Then, we model the SF of this component as

$$\mathrm{SF}_{ej}(v, a) = \frac{1}{1 + \left(\frac{v}{a}\right)^{\gamma}}. \tag{17}$$

The survival function of the total velocity distribution is thus

$$\begin{aligned}\mathrm{SF}(v) = {} & f_{\mathrm{bound}}\mathrm{SF}_b(v, a_b) \\ & + f_{\mathrm{unbound}}\mathrm{SF}_{ub}(v, a_{ub}) \\ & + f_{ej}\mathrm{SF}_{ej}(v, a_{ub}),\end{aligned} \tag{18}$$

where $f_{\mathrm{bound}} + f_{\mathrm{unbound}} + f_{ej} = 1$. Note that the bound component with f_{bound} and σ_b is measured directly from the stellar distribution (see Figs 3 and 4). For the second component, even though we have left a_{ub} as a free parameter, we have found that this parameter is well represented by the scale parameter obtained using the velocity dispersion of the parent clump, σ_{cl}. Then, the fitting procedure is dominated by the ejected component described in equation (17) and its weight, i.e. γ and f_{ej}. For the scale parameter of this component, we have used the same as for the unbound, a_{ub}, since we want the power-law signature to be fully developed at the velocity when the unbound Maxwell–Boltzmann distribution becomes unimportant.

Fig.13(b) shows the time evolution of γ and f_{ej}. The evolution of f_{ej} shows how the fraction of dynamically ejected stars grows with time. Small clusters with $M_{cl} = 300\,\mathrm{M}_\odot$ show larger f_{ej} values, with a similar evolution independent of ϵ_{ff}, but mostly dependent of the age of the clusters and the initial density. At 20 Myr, these small clusters reach $f_{ej} \sim 0.08-0.2$ for low-Σ_{cloud} models and 0.25−0.45 in the high-Σ_{cloud} case. As M_{cl} increases, the importance of the ejected population decreases to a range between 0.01 and 0.1 for $M_{cl} = 3000\,\mathrm{M}_\odot$ and between 0.001 and 0.04 in the most massive clusters.

However, we find no clear trend for the evolution of the power-law parameter γ, with neither M_{cl} or ϵ_{ff}. Rather than being dependent of global parameters, γ is more likely to depend on the population of binaries as shown by Perets & Šubr (2012). In our case, we obtained an average value of $\gamma = 1.6 \pm 0.4$.

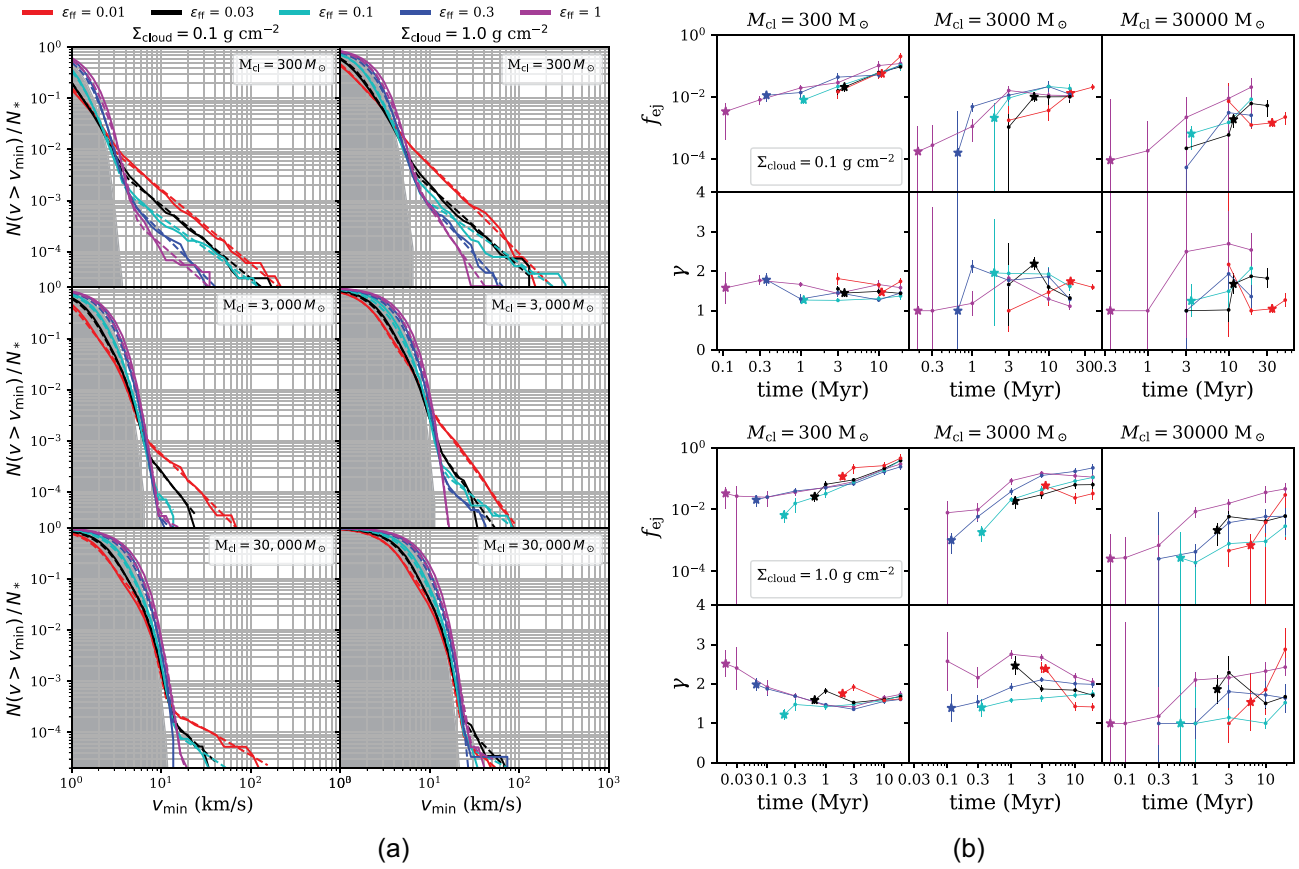

Figure 13. (a) Evolution of the transverse, i.e. 2D, high-velocity cumulative distributions normalized by the total number of stars in the clusters measured at $t = t_*$. Shaded area shows the respective Maxwell–Boltzmann distribution with σ equal to the initial mass-averaged velocity dispersion of the clump. Rows arrange different parent clump masses, M_{cl} while columns arrange the low (left) and high (right) Σ_{cloud} cases. Note, stellar remnants are not included in this graph. This figure is equivalent to fig. 10 of Farias et al. (2020), where we make direct comparison of our simulations with estimates for the Orion Nebula Cluster. (b) Fitting parameters at different times for the excess in the velocity distribution of modelled star clusters, f_{ej} (top rows) and γ (bottom rows) for simulations in the high-Σ_{cloud} (top set of panels) and low-Σ_{cloud} (bottom set of panels) regimes. Star symbols show the time at which star formation is finished, where the corresponding fitting model is shown in figure (a). Fitting is made at different times starting from $t = t_*$. Note that the large errorbars represent times where fitting the excess is uncertain given that is not yet fully developed, e.g. see the high-Σ_{cloud} case of $M_{cl} = 3000\,M_\odot$ and $\epsilon_{ff} = 1$, i.e. magenta line in the lower right panel of figure (a).

4.6 Runaway stars

While the above description is useful at characterizing the different components of the stellar distribution, compiling such population data is challenging, especially for the high-velocity lower mass stars that are now far from their origins and thus hard to find and link to a given population. However, isolated runaway stars are easier to find, especially O and B stars. Observations of O and B runaway stars indicate that between 10–30 per cent of O stars and 2–10 per cent of B stars are runaways (Gies 1987; Stone 1991; de Wit et al. 2005), depending on precise definition of this class.

Fig. 14 shows the percentage of ejected stars per model without a velocity cut-off (filled circles), and with velocities above 20 km s^{-1} that we adopt as a definition for a runaway star. These numbers represent only dynamically ejected stars via strong interactions or rapid change in the cluster potential, excluding supernovae related ejections.

We show the results for three ranges of mass: all stars in the system (left-hand column); O stars (middle column); and B stars (right-hand column). As found in our previous work in Paper II, there is a modest increase in the fraction of overall ejected stars with ϵ_{ff}, shown in the first column of Fig. 14 as filled circles, which is a result of the increasingly rapid depletion of the background gas.

The results for high-velocity runaway stars appear to be divided into two regimes, determined by Σ_{cloud}. In the low-Σ_{cloud} case (top panels), slowly forming clusters appear to form slightly higher fractions of runaway stars at all masses, especially for the most massive clusters. However, the differences are modest and within the uncertainties.

With the exception of the `m300L` case at $\epsilon_{ff} = 0.01$, we find more O runaway stars when ϵ_{ff} approaches to 0.01, as expected given the longer time stars remain in a dense state during the formation phase, but increase again when $\epsilon_{ff} = 1$. The former is a consequence of the high peak density reached at the beginning, given that all stars formed in half a free-fall time and collapse into the centre together.

For B stars, the fraction of runaway stars appears to be independent of ϵ_{ff}, but with strong dependence on M_{cl}. Small clusters, with higher initial densities, form higher fractions of B star runaways than the most massive clusters. If fact, in the low-Σ_{cloud} case `m30000L` models form no runaways in the B mass range, except for the slowly forming case with $\epsilon_{ff} = 0.01$.

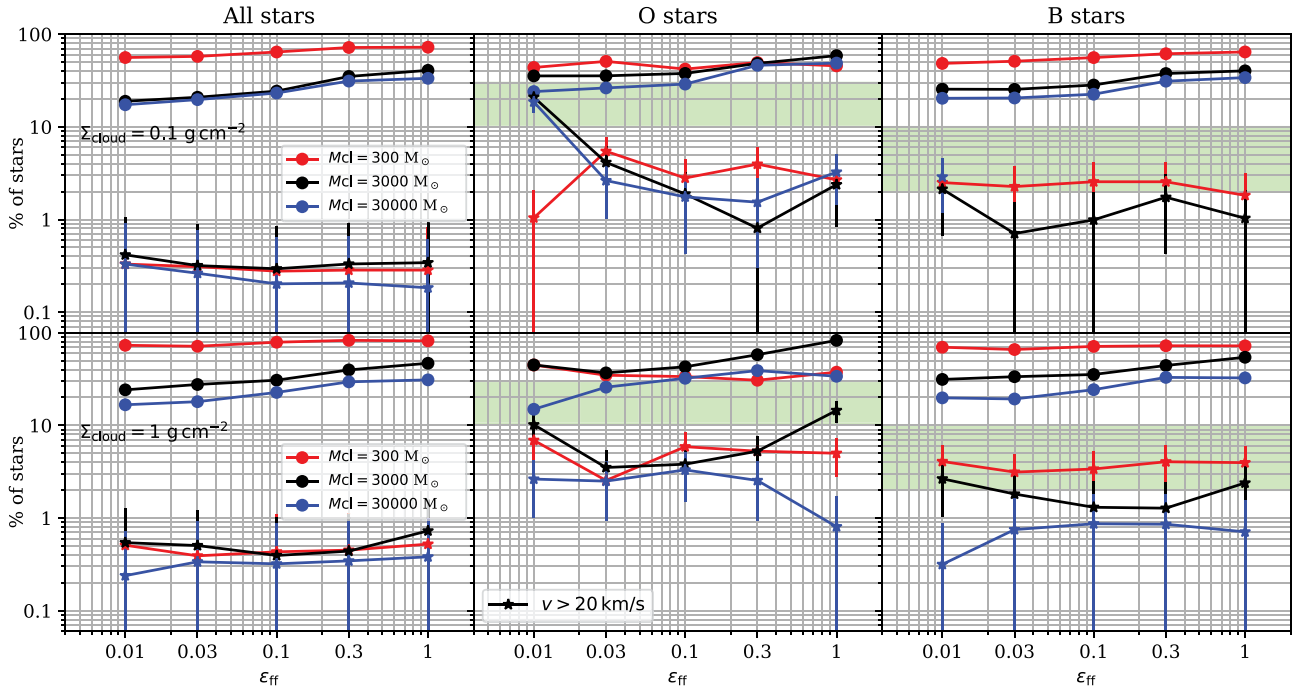

Figure 14. Percentage of ejected stars relative to all stars in each mass range for the low (top panels) and high (bottom panels) Σ_{cloud} cases measured at 20 Myr. The first column shows the results when using all stars in the set. The second and third columns show the fraction of O and B dynamically ejected stars, respectively. Shaded areas in these panels show the range of observed values (see the text).

In the high-Σ_{cloud} case, results appear to be dominated by the high-density environment, and similar fractions of runaway stars are found in each model. In this case, B star runaways are found in all models, but the trend remains the same as more massive clusters produce smaller fractions of B star runaways.

About 2 and 4 per cent of B stars are ejected with high velocities for the low- and high-Σ_{cloud} cases, respectively. These figures are consistent with the range of values found for B stars (see e.g. Eldridge, Langer & Tout 2011). Increasing M_{cl} brings down the number of high-velocity B star runaways down to 0.5–1 per cent in the high-Σ_{cloud} case, and none in the low-Σ_{cloud} case (with the exception of the $\epsilon_{ff} = 0.01$ case, where we find 2 per cent). These results highlight the high densities reached by the low-mass clusters at formation, but the subsequent quick expansion implies that most of these high-velocity ejections happened very early in the evolution of these systems.

4.6.1 *Interaction rates to produce dynamical ejections*

We estimate the number of ejected stars we expect at a given time, given the dynamical history of a star cluster. For single stars, we can estimate the cross-section πb^2 of interactions that result in a closest approach of b_{min}, where the velocity reaches a value of v_{max}. For two stars approaching from infinity with relative velocity σ and impact parameter b, energy and angular momentum conservation implies that a star reaches a closest approach at a maximum velocity v_{max} when

$$b = \frac{2Gm_t}{(v_{max}^2 - \sigma^2)} \frac{v_{max}}{\sigma}, \tag{19}$$

where m_t is the total mass of the interacting stars. Note that this result is only valid for $v_{max} \geq \sigma$. The v_{max}/σ factor is the gravitational focusing factor, which increases the impact parameter b in low-velocity environments. Then, the interaction rate for interactions that can potentially eject a star, is given by $\pi b^2 \times n_s \times \sigma$, i.e.

$$\Gamma = 4\pi n_s \sigma \left[\frac{Gm_t}{(v_{max}^2 - \sigma^2)} \frac{v_{max}}{\sigma} \right]^2. \tag{20}$$

The total number of interactions that will accelerate stars up to v_{max}, from $t = 0$ to $t = T$ is

$$N_{int} = \int_0^T \sum_{i=1}^{N} \Gamma_i(t) \mathrm{d}t, \tag{21}$$

where Γ_i is the interaction rate of each star in the system. This number should be proportional to the number of observed runaway stars with escape velocities $v > v_{max}$, i.e. N_v. We calculate this proportionality factor in our models by numerically integrating equation (21) and then comparing to the number of runaway stars ejected with velocities greater than 20 km s^{-1}. Specifically, we numerically integrate equation (21) over time for each individual simulation at each snapshot, constructing tracks in the N_{int}–velocity plane. We calculate Γ_i using global values of σ and n_s, based on the stellar population within the half-mass radius of the system. We consider as runaway stars any star with $v > v_{max} = 20$ km s^{-1} that is not a stellar remnant. To avoid contamination of stars close to the centre of the potential well, where local escape velocities may be large due episodic close encounters, we only consider stars beyond 2 stellar half-mass radius when counting the number of runaway stars. We combine the results of each set of models by placing all N_{int}–v data pairs of each simulation at each snapshot on a single combined set. We divided this set in N_{int} bins of equal number of data points and take the average of N_v. Fig. 15 shows these results for all the different sets of models in this work. It is expected that $N_{int} \propto N_v$ and this is approximately seen in Fig. 15. From these results, we calculate a

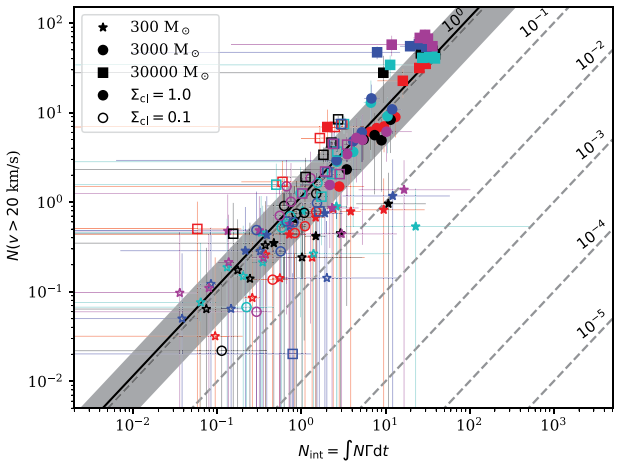

Figure 15. $N_{\rm int}$ versus the number of dynamically ejected high-velocity stars, collected for all models in this work. Each point represents the average number of high-velocity stars for measurements with the same $\epsilon_{\rm ff}$ and $M_{\rm cl}$ that fall in the same $N_{\rm int}$ bin.

proportionality factor $\eta = 1.15^{+1.0}_{0.7}$. This shows that the number of runaway stars is a direct constraint on the dynamical history of a star cluster. For instance, this linear relation indicates that if a star cluster is characterized with 10 stars with $v > 20\,{\rm km\,s^{-1}}$, then models trying to reproduce such a system must reach the same number of strong interactions (on average) during its age.

5 DISCUSSION

We have expanded our modelling of star cluster formation to cover a wide range of masses of initial gas clumps and studied their resulting star clusters. This step is important to eventually produce a comprehensive grid of models that could be applied to interpret populations of star clusters. Given the assumptions of the turbulent clump model, certain scalings of properties occur as a function of clump mass (at fixed mass surface density of surrounding cloud environment). These scalings, e.g. of density, velocity dispersion, etc., have implications for the dynamical evolution of the resulting stellar system, for instance, affecting the relaxation time and degree of binary processing.

The evolution of cluster radii (e.g. half-mass radii of the bound components) and radial profiles with time are metrics that can be compared to observed systems, although this will typically be best achieved by converting model mass profiles into multiwavelength light profiles. In our modelling programme, this step is deferred to a future paper in the series, requiring implementation of pre-main-sequence evolutionary tracks into the simulation framework. However, in principle, a cluster that is observed to have a given (mean) age, mass, half-mass (or light) radius, and radial mass (or light) profile can be compared with the outputs of the models presented here. There will be a range of formation parameters ($M_{\rm cl}$, $\Sigma_{\rm cloud}$, ϵ, $\epsilon_{\rm ff}$, etc.) that are consistent with a given set of observational data. The grid of models presented here is a first step in the process of building tools that will eventually allow constraints to be placed on formation parameters from observed clusters, which could then be used to estimate initial cluster and clump mass functions and distributions of $\Sigma_{\rm cloud}$ formation environments.

We find variations in cluster sizes with $\epsilon_{\rm ff}$ for models of the same initial mass and environmental mass surface density. This is due to the potential of the natal gas clump restricting the expansion that arises from the initially supervirial state. However, these differences in sizes are most apparent only for a relatively short time period similar to the star formation time, since after this rapid cluster expansion occurs and the various models tend to converge to have similar sizes at a given age.

Given such degeneracies, direct measures of $\epsilon_{\rm ff}$, i.e. via measurement of age spreads, remains important. However, accurately measuring age spreads in young star clusters is a challenge that involves model-dependent fitting to pre-main-sequence evolutionary tracks (e.g. Tognelli, Prada Moroni & Degl'Innocenti 2011; Bressan et al. 2012; Baraffe et al. 2015) and is also complicated by observational uncertainties in extinction, photometric variability and unresolved multiplicity (e.g. Da Rio et al. 2016). Associating individual runaway stars with a given young cluster and/or spreads in kinematic expansion ages is another, more direct, method for estimating $\epsilon_{\rm ff}$ (e.g. Tan 2006; Farias et al. 2020).

We have shown that properties that depend on the time-integrated density of the stellar systems, i.e. amount of binary processing and fraction of dynamically ejected stars, do have significant sensitivity to $\epsilon_{\rm ff}$. These tend to show the strongest variations in small clusters, due to their short relaxation times. However, testing models via observations of such clusters faces the inherent problem of small numbers of stars leading to larger sampling uncertainties. Overcoming this would require observations of large numbers of low-mass clusters.

Independent from $\epsilon_{\rm ff}$, we have found significant variations of behaviour between low-mass and high-mass forming clusters, which are mostly due to the differences in their relaxation times during the formation phase. Even slowest forming ($\epsilon_{\rm ff} \sim 0.01$) low-mass clusters evolve to have relatively low bound mass fractions ($\lesssim$0.6 for $\Sigma_{\rm cloud} = 0.1\,{\rm g\,cm^{-2}}$; $\lesssim$0.4 for $\Sigma_{\rm cloud} = 1.0\,{\rm g\,cm^{-2}}$) by $\sim$20 Myr and that are continuing to decline quickly, while in the higher mass systems $f_{\rm bound}$ can remain as high as $\sim$0.8 at these times and with much more gradual rates of decline. Related to this, lower mass clusters are able to form a more significant high-velocity population of dynamically ejected stars. While all of the clusters show mass segregation leading to a more top heavy high-mass end MF slope in their bound, central components, this effect is stronger in lower mass clusters. Finally, the average system mass in the bound remnants of low-mass clusters shows significant evolution to higher values, partly driven by significant numbers of dynamically formed binaries. In more massive clusters, such binary formation is rare and binary processing tends to destroy the primordial binary population, e.g. from $f_{\rm bin}$ of 1/2 down to as low as $\sim$1/3 in the most massive, highest density clusters considered. These are significant variations that may be testable by future observations of young clusters.

There are a number of caveats and limitations of the models that we have presented. The protocluster models are globally spherically symmetric and lack spatial and kinematic substructure that might be expected to arise from interstellar turbulence. Allowing for such features is planned in future papers in this series. Furthermore, in the models presented here, higher order multiples were not part of the initial conditions set-up and their formation by capture was negligible. If significant fractions of triple and higher order multiple systems are found to exist in young clusters, then this would indicate a need to incorporate such systems as part of the primordial population.

6 CONCLUSIONS

We have presented a set of star cluster formation simulations that span a wide range of initial clump masses ($M_{\rm cl}$ from 300 to 30 000 $M_\odot$), cloud environment mass densities ($\Sigma_{\rm cloud}$ from 0.1 to 1.0 g cm^{-2}) and star formation efficiencies per free-fall time ($\epsilon_{\rm ff}$ from 0.01 to 1.0). These simulations, all involving global star formation efficiency of 50 per cent and all starting with 50 per cent primordial binaries, follow the *N*-body dynamics of the stellar populations, including evolution of the bound cluster, binary properties, mass segregation, and production of high-velocity runaways.

We summarize our main results as follows:

(i) Bound mass fractions at the end of star formation are similar in all models, i.e. around 90 per cent (see Section 4.1). However, the subsequent evolution diverges dramatically depending on $M_{\rm cl}$ and $\Sigma_{\rm cloud}$, with low-mass clusters in high-density environments retaining the smallest fractions ($f_{\rm bound} \lesssim 0.3$) in their remnant bound cores. In general, slowest forming clusters retain higher bound fractions.

(ii) The evolution of half-mass radii of the bound clusters also shows large differences in behaviour depending on cluster mass and environment. Low-mass clusters in high-density environments undergo the largest degree of expansion during the first 20 Myr of evolution, since they form relatively quickly and have short relaxation times that drive this dynamical evolution. Variations with $\epsilon_{\rm ff}$ are mostly related to the length of the formation phase, during which the gravitational potential of the gas clump acts to confine the cluster, retarding its expansion. Once the gas is exhausted, clusters can enter a PFS phase, during which they have relatively constant sizes (see Section 4.1 and Fig. 5). This phase ends once the cluster has had time to undergo dynamical relaxation, which leads to further expansion. This delay in expansion means that clusters of a given $M_{\rm cl}$ and $\Sigma_{\rm cloud}$ have similar sizes by a time of ~ 20 Myr.

(iii) The core radius evolution is independent of $\epsilon_{\rm ff}$ and remains relatively constant for about one crossing time. If gas is still present in the system, the core radius can remain dense for longer (i.e. $\epsilon_{\rm ff} < 0.03$). The expansion of the core radius sets the end of the PFS phase that star clusters undergo after gas expulsion.

(iv) The above results imply that binary systems are disrupted efficiently in the most massive cluster during the initial ~20 Myr period that has been modelled here. However, in lower mass systems, binary disruption is constrained to the formation time only, given their quick post-gas-expulsion expansion (see Section 4.3). Most disrupted binaries have semimajor axes greater than 100–1000 au, depending on $\Sigma_{\rm cloud}$ (Fig. 10). Lower mass systems can disrupt harder binaries relative to the most massive clusters, given their high initial densities. Binary formation by capture is more efficient in lower mass systems (see Fig. 9). By 20 Myr about 6–8 per cent of binaries are formed by capture in the bound systems. This figure drops dramatically for clusters with $M_{\rm cl} = 3000\,M_\odot$, i.e. is below 1 per cent and practically zero in more massive systems. Binaries formed by capture are concentrated at higher end of the semimajor axis distribution, showing a noticeable secondary peak in at $a = 10^5$ au at 20 Myr. These binaries are formed mainly after gas expulsion during the expansion of the cluster.

(v) Young star clusters develop different levels of central mass segregation reaching a peak at the time the core radius begins to expand (see Section 4.4). The short dynamical time-scales of clusters with $M_{\rm cl} = 300\,M_\odot$ and small IMF sampling causes these systems evolve to have the most top heavy central regions in relation to their outskirts.

(vi) The fraction of dynamically ejected stars depends on the initial mass of the clump and the mass surface density of its environment (Section 4.6). Low-mass clusters produce greater fractions of ejected stars, i.e. ranging from 8 to 20 per cent in the low-$\Sigma_{\rm cloud}$ case and 25 to 45 per cent in the high-$\Sigma_{\rm cloud}$ case.

(vii) The percentage of runaway stars, i.e. dynamically ejected stars, follows the same dependence, but differences are modest. B stars, however, show the greatest differences across $M_{\rm cl}$, where low-mass clusters are able to reproduce observed percentages, with an average of 2.5 per cent in the low-$\Sigma_{\rm cloud}$ case and 4 per cent in the high-density environment.

ACKNOWLEDGEMENTS

JPF was supported by NSF Career grant no. 1748571 and NASA grant 80NSSC20K0507. JPF and JCT acknowledge support from ERC Advanced Grant project MSTAR.

DATA AVAILABILITY

The data underlying this article will be shared on reasonable request to the corresponding author.

REFERENCES

Aarseth S. J., 2003, Gravitational N-Body Simulations. Cambridge Univ. Press, Cambridge
Banerjee S., Kroupa P., Oh S., 2012, ApJ, 746, 15
Baraffe I., Homeier D., Allard F., Chabrier G., 2015, A&A, 577, A42
Binney J., Tremaine S., 2008, Galactic Dynamics: Second Edition. Princeton Univ. Press, Princeton, NJ
Bressan A., Marigo P., Girardi L., Salasnich B., Dal Cero C., Rubele S., Nanni A., 2012, MNRAS, 427, 127
Butler M. J., Tan J. C., 2012, ApJ, 754, 5
Casertano S., Hut P., 1985, ApJ, 298, 80
Cunningham A. J., Klein R. I., Krumholz M. R., McKee C. F., 2011, ApJ, 740, 107
Dale J. E., Ercolano B., Bonnell I. A., 2015, MNRAS, 451, 987
Da Rio N. et al., 2016, ApJ, 818, 59
de Wit W. J., Testi L., Palla F., Zinnecker H., 2005, A&A, 437, 247
Dowell J. D., Buckalew B. A., Tan J. C., 2008, AJ, 135, 823
Eldridge J. J., Langer N., Tout C. A., 2011, MNRAS, 414, 3501
Elson R. A. W., Fall S. M., Freeman K. C., 1987, ApJ, 323, 54
Farias J. P., Tan J. C., Chatterjee S., 2017, ApJ, 838, 116
Farias J. P., Tan J. C., Chatterjee S., 2019, MNRAS, 483, 4999
Farias J. P., Tan J. C., Eyer L., 2020, ApJ, 900, 14
Federrath C., Schrön M., Banerjee R., Klessen R. S., 2014, ApJ, 790, 128
Gavagnin E., Bleuler A., Rosdahl J., Teyssier R., 2017, MNRAS, 472, 4155
Geen S., Hennebelle P., Tremblin P., Rosdahl J., 2015, MNRAS, 454, 4484
Gies D. R., 1987, ApJS, 64, 545
Ginsburg A., Bressert E., Bally J., Battersby C., 2012, ApJ, 758, L29
Gutermuth R. A., Megeath S. T., Myers P. C., Allen L. E., Pipher J. L., Fazio G. G., 2009, ApJS, 184, 18
Hansen C. E., Klein R. I., McKee C. F., Fisher R. T., 2012, ApJ, 747, 22
Hobbs G., Lorimer D. R., Lyne A. G., Kramer M., 2005, MNRAS, 360, 974
Hurley J. R., Pols O. R., Tout C. A., 2000, MNRAS, 315, 543
Hurley J. R., Tout C. A., Pols O. R., 2002, MNRAS, 329, 897
Kroupa P., 2001, MNRAS, 322, 231
Kuhn M. A., Hillenbrand L. A., Sills A., Feigelson E. D., Getman K. V., 2019, ApJ, 870, 32
Lada C. J., Lada E. A., 2003, ARA&A, 41, 57
McKee C. F., Tan J. C., 2003, ApJ, 585, 850
Matzner C. D., McKee C. F., 2000, ApJ, 545, 364

Mueller K. E., Shirley Y. L., Evans N. J., II, Jacobson H. R., 2002, ApJS, 143, 469
Nakamura F., Li Z.-Y., 2007, ApJ, 662, 395
Nakamura F., Li Z.-Y., 2014, ApJ, 783, 115
Offner S. S. R., Moe M., Kratter K. M., Sadavoy S. I., Jensen E. L. N., Tobin J. J., 2022, preprint (arXiv:2203.10066)
Oh S., Kroupa P., 2016, A&A, 590, A107
Perets H. B., Šubr L., 2012, ApJ, 751, 133
Peters T., Banerjee R., Klessen R. S., Mac Low M.-M., Galván-Madrid R., Keto E. R., 2010, ApJ, 711, 1017
Peters T., Banerjee R., Klessen R. S., Mac Low M.-M., 2011, ApJ, 729, 72
Proszkow E.-M., Adams F. C., 2009, ApJS, 185, 486
Qian P. X., Cai M. X., Zwart S. P., Zhu M., 2017, Publ. Astron. Soc. Pac., 129, 094503
Raghavan D. et al., 2010, ApJS, 190, 1
Reggiani M. M., Meyer M. R., 2011, ApJ, 738, 60
Rogers H., Pittard J. M., 2013, MNRAS, 431, 1337
Stone R. C., 1991, AJ, 102, 333
Tan J. C., 2006, Proc. IAU Symp. 2, Massive Star and Star Cluster formation. Cambridge Univ. Press, Cambridge, p. 258
Tan J. C., Beltrán M. T., Caselli P., Fontani F., Fuente A., Krumholz M. R., McKee C. F., Stolte A., 2014, in Protostars Planets VI. Univ. Arizona Press, Tucson, AZ, p. 149
Tanaka K. E. I., Tan J. C., Zhang Y., 2017, ApJ, 835, 32
Tognelli E., Prada Moroni P. G., Degl'Innocenti S., 2011, A&A, 533, 1
Wang L., Spurzem R., Aarseth S., Nitadori K., Berczik P., Kouwenhoven M. B. N., Naab T., 2015, MNRAS, 450, 4070

APPENDIX A: ANCILLARY RESULTS FOR THE FULL SET OF BINARY PROPERTIES

Here, we present results related to binary properties over the full range of $M_{\rm cl}$, $\Sigma_{\rm cloud}$, and $\epsilon_{\rm ff}$ explored in our grid of models. Figure A1 and A2 shows binary properties for $M_{\rm cl} = 300$ M$_\odot$ clouds, for all $\epsilon_{\rm ff}$ used in this work in the low-$\Sigma_{\rm cloud}$ and high-$\Sigma_{\rm cloud}$ cases respectively. Figures A3 and A4 shows the same properties but for clouds with $M_{\rm cl} = 3{,}000$ M$_\odot$ in the low and high-$\Sigma_{\rm cloud}$ respectively. The same set of parameters is shown in Figures A5 and A6 but for clouds with $M_{\rm cl} = 30{,}0000$ M$_\odot$.

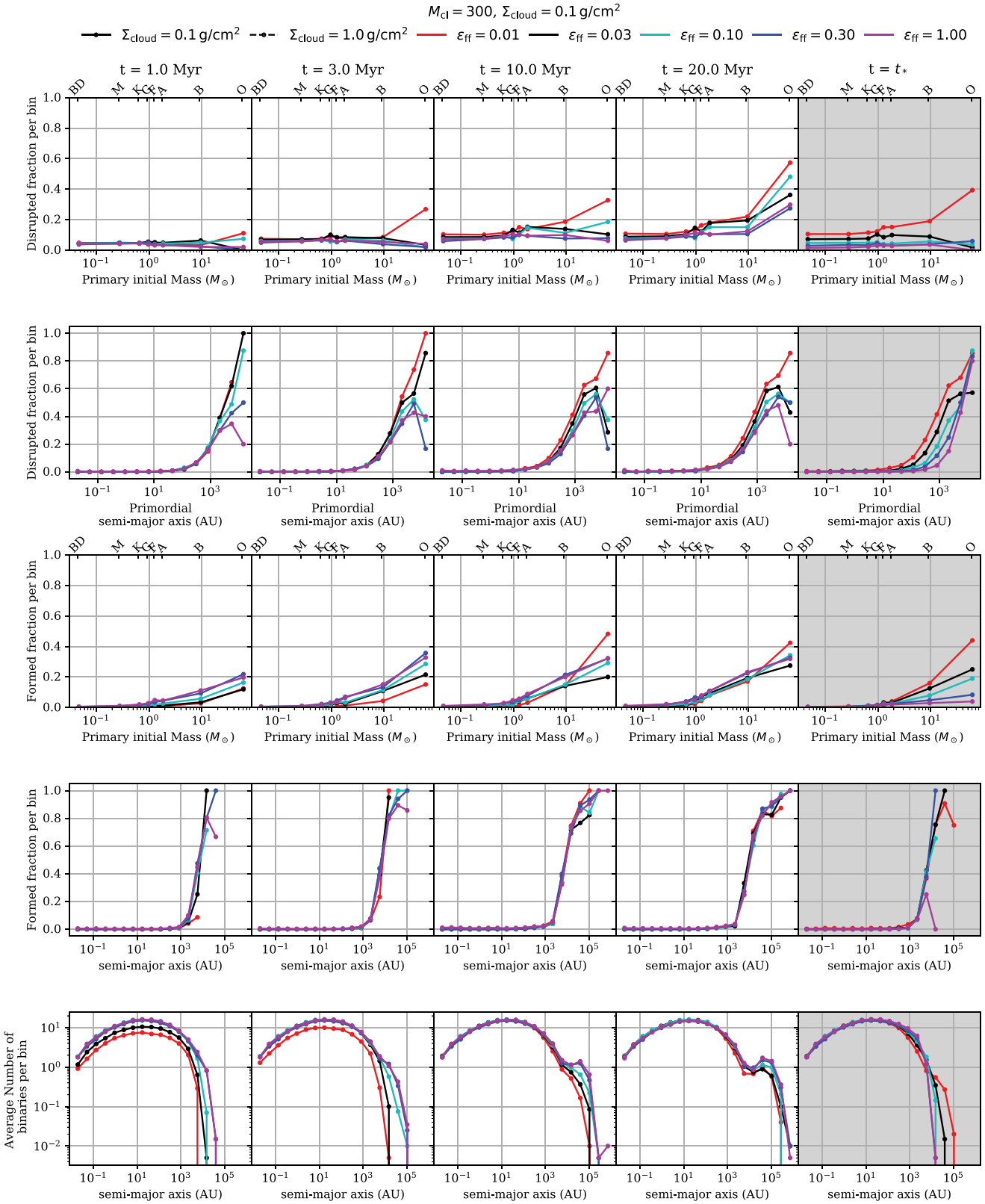

Figure A1. Same as Fig. 10 but for models with $M_{cl} = 300\,M_\odot$ and with $\Sigma_{cloud} = 0.1\,g\,cm^{-2}$ and $\epsilon_{ff} = 0.01\,g\,cm^{-2}$, 0.03, 0.1, 0.3, and 1.0.

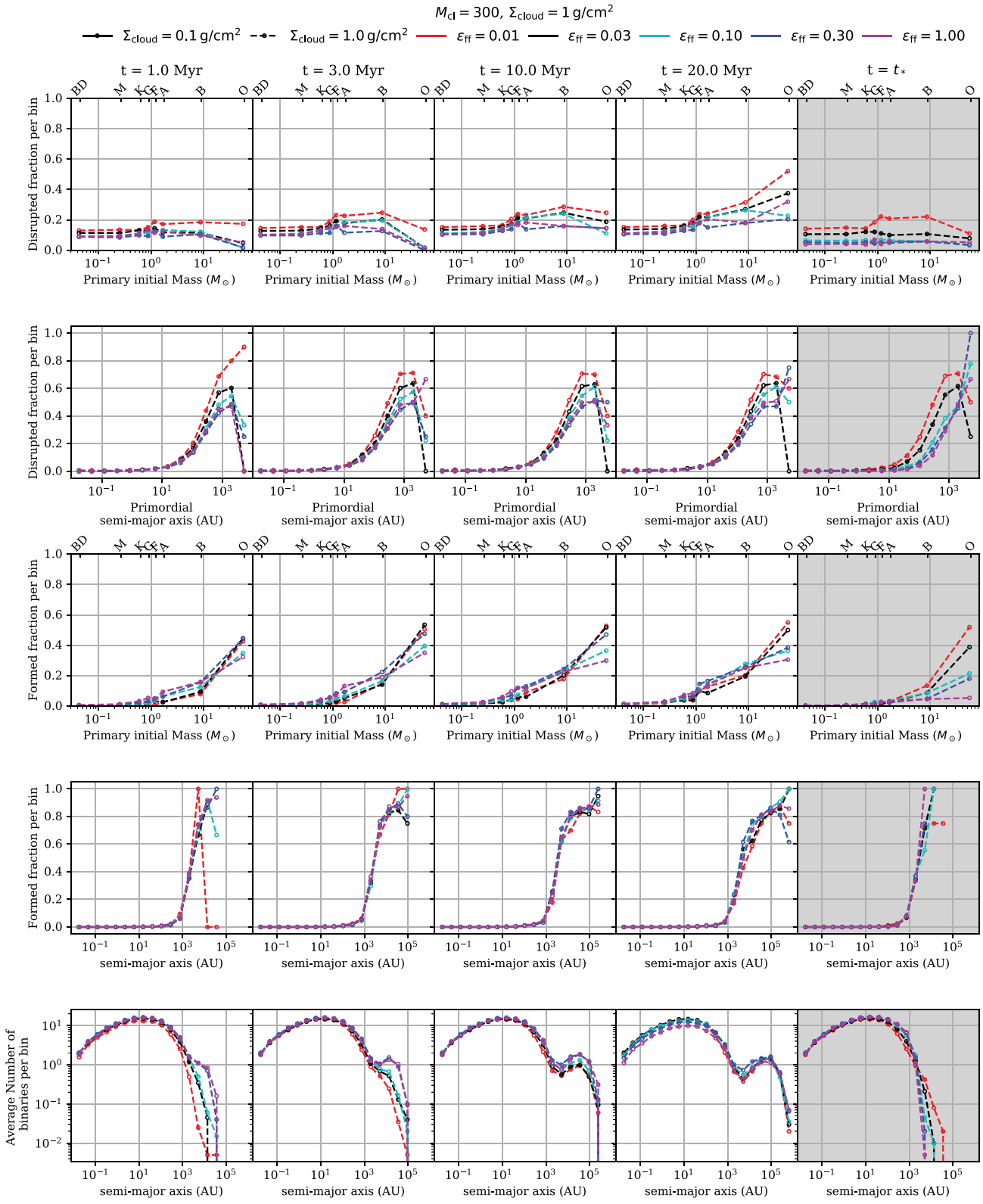

Figure A2. Same as Fig. A1 but for models with $\Sigma_{cloud} = 1.0\,g\,cm^{-2}$.

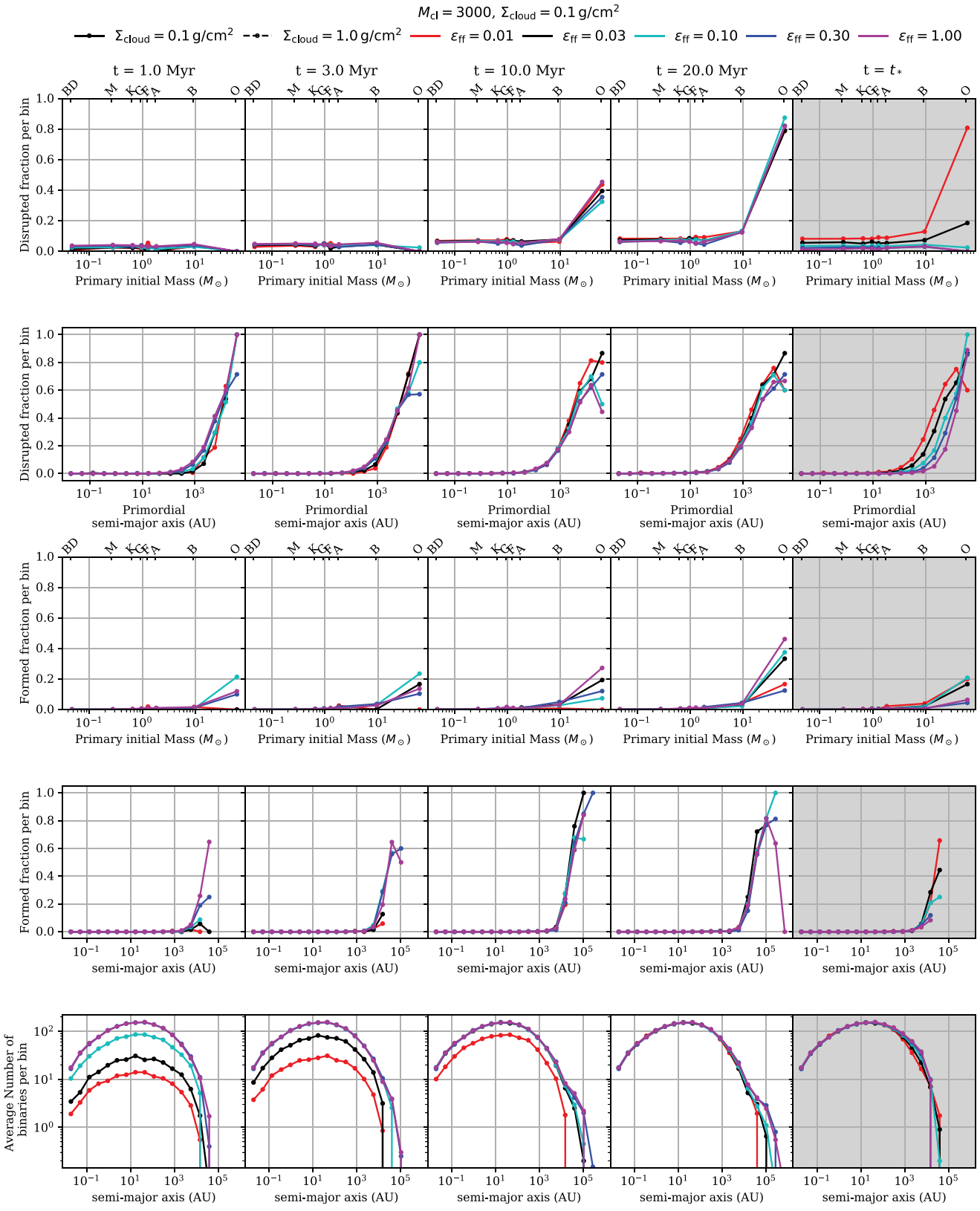

Figure A3. Same as Fig. A1 but for models with $M_{cl} = 3,000\,M_\odot$ and $\Sigma_{cloud} = 0.1\,g\,cm^{-2}$.

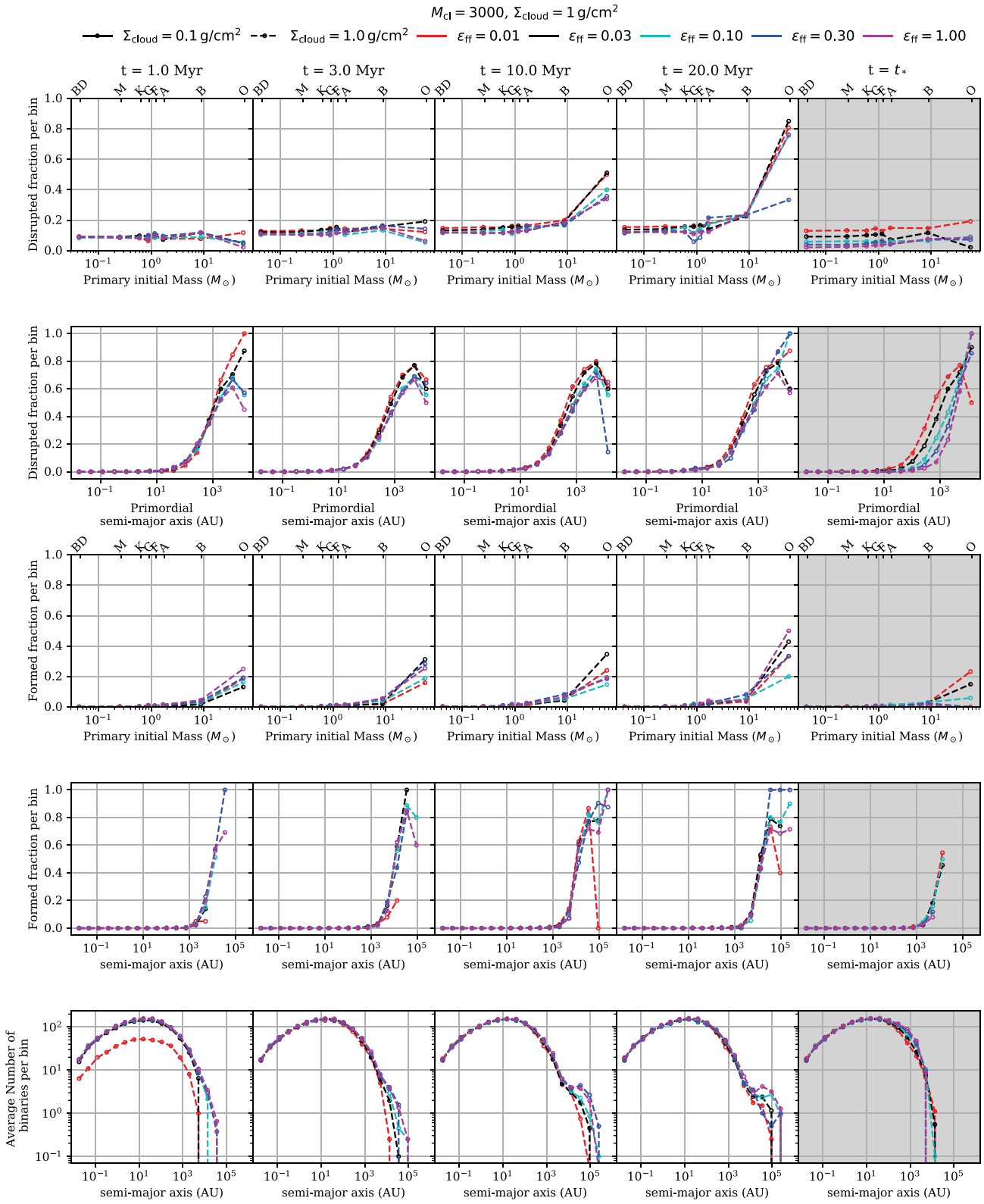

Figure A4. Same as Fig. A3 but for models with $\Sigma_{cloud} = 1.0\,g\,cm^{-2}$.

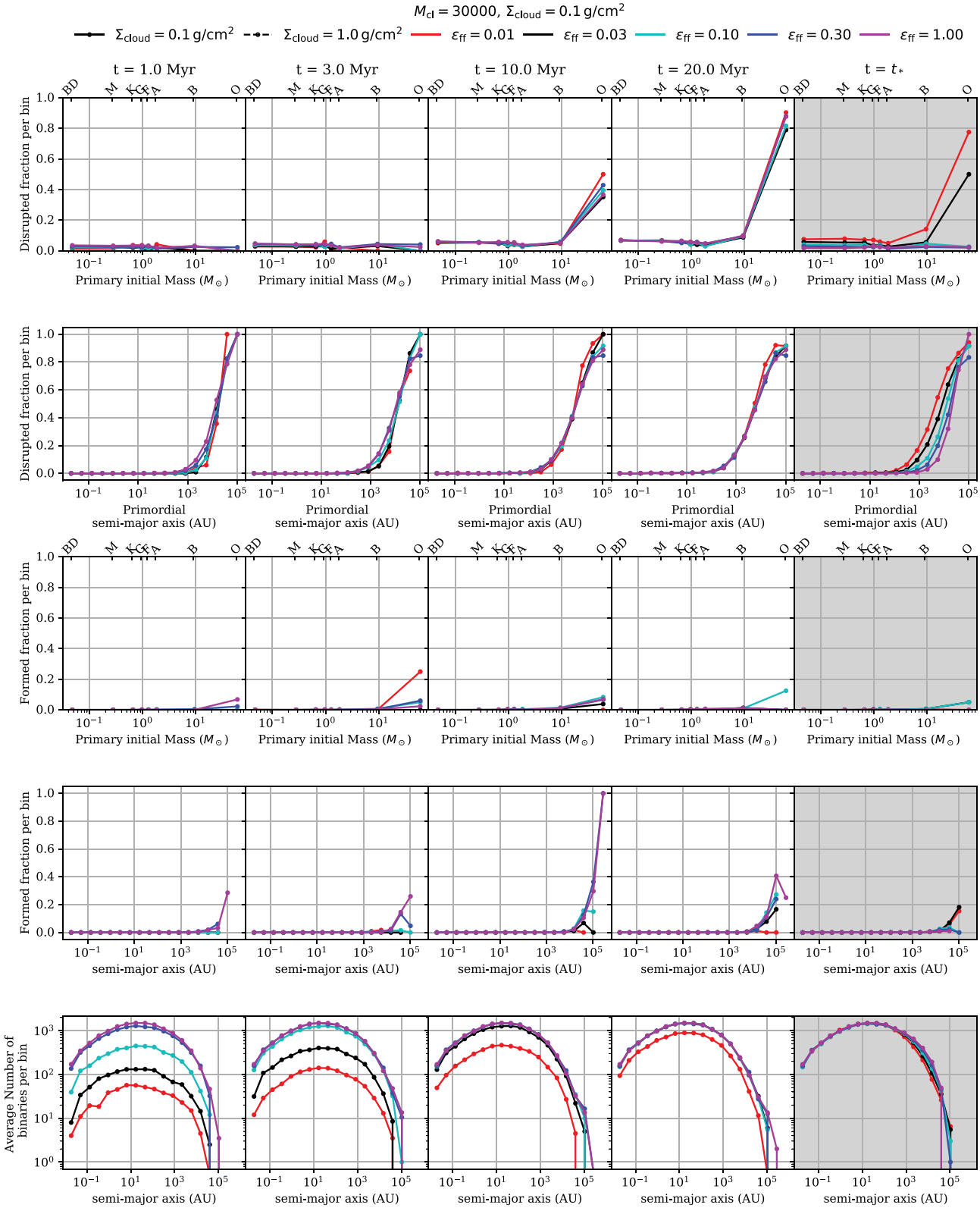

Figure A5. Same as Fig. A3 but for models with $M_{cl} = 30\,000\,M_\odot$ and $\Sigma_{cloud} = 0.1\,g\,cm^{-2}$.

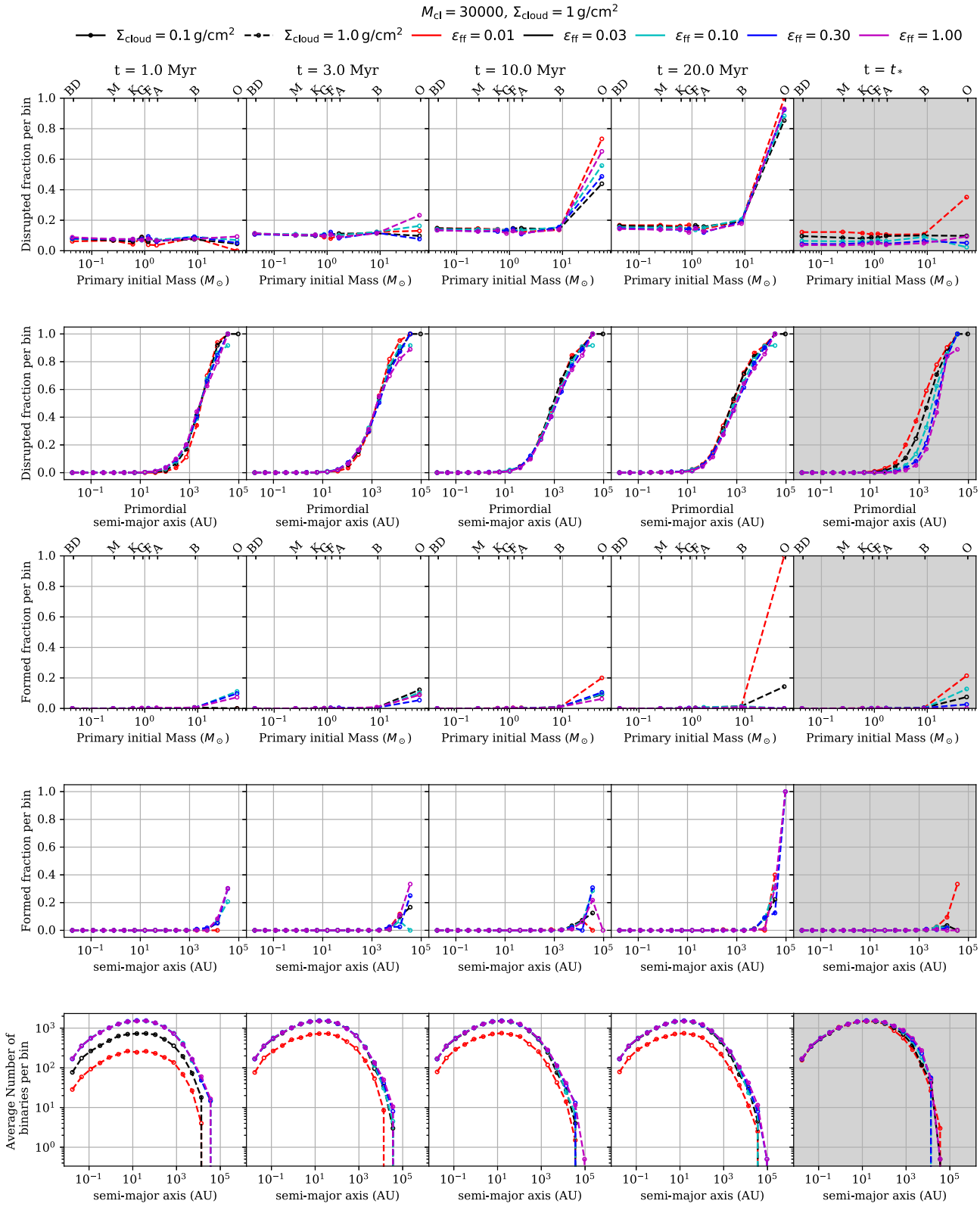

Figure A6. Same as Fig. A5 but for models with $\Sigma_{cloud} = 1.0\,g\,cm^{-2}$.

This paper has been typeset from a TEX/LATEX file prepared by the author.